DEPARTMENT OF ELECTRICAL
AND COMPUTER ENGINEERING

NOVA SCHOOL OF
SCIENCE & TECHNOLOGY

JOÃO AFONSO DAS NEVES SANTOS BICHO VICENTE
Bsc in Electrical and Computer Engineering

TECHNO-ECONOMIC ASSESSMENT OF A SUPERCONDUCTING FAULT CURRENT LIMITER FOR WIND FARM GRID INTEGRATION: A CASE STUDY IN PORTUGAL

MASTER IN ELECTRICAL AND COMPUTER ENGINEERING

NOVA University Lisbon
September, 2025

DEPARTMENT OF ELECTRICAL
AND COMPUTER ENGINEERING

TECHNO-ECONOMIC ASSESSMENT OF A SUPERCONDUCTING FAULT CURRENT LIMITER FOR WIND FARM GRID INTEGRATION: A CASE STUDY IN PORTUGAL

JOÃO AFONSO DAS NEVES SANTOS BICHO VICENTE

Bsc in Electrical and Computer Engineering

Adviser: João Murta Pina
Associate Professor, NOVA School of Science and Technology

Co-adviser: Nuno Manuel Ortega Amaro
Assistant Professor, NOVA School of Science and Technology

MASTER IN ELECTRICAL AND COMPUTER ENGINEERING

NOVA University Lisbon
September, 2025

Techno-Economic Assessment of a Superconducting Fault Current Limiter for Wind Farm Grid Integration: A Case Study in Portugal

Em honra ao meu primo Francisco.

Acknowledgements

Today, an important chapter of my life comes to a close. Over the past seven years, I have faced countless challenges, grown both personally and academically, and could not be more proud of that journey. However, this beautiful path was not written by me alone.

Firstly, I would like to express my sincere gratitude to my advisors, Professor João Murta Pina and Professor Nuno Amaro, for their constant availability, support, and insightful knowledge throughout the course of this dissertation.

To all of my fellow course colleagues and friends, I feel nothing but pride to have shared this beautiful journey with you. The memories we've created together will stay with me forever, and I am truly grateful for every moment.

To my childhood best friend — more than a friend, a true brother. I am so proud of us. Nearly twenty years of this beautiful friendship have shaped who I am, and I am deeply grateful I had the privilege of growing up alongside you.

To all my dearest friends whom I had the privilege of meeting during my Erasmus in Budapest, thank you for making those five months the most unforgettable of my life. You will always hold a special place in my heart.

A special mention and heartfelt greetings are extended to my dear colleagues and friends at EDP, whose support during the final stages of this dissertation was the motivation I most needed.

Finally, to the backbone of my life — my family. Thank you for your unconditional love, endless patience, and unwavering belief in me. None of this would have been possible without your constant support.

As every chapter comes to an end, a new one always begins.

> *"Whatever you do in this life, it's not legendary,*
> *unless your friends are there to see it."*
>
> **— Barney Stinson**, Best friend, Best man, Father.

Abstract

The integration of new renewable energy sources, particularly wind farms, into existing power grids presents significant technical challenges due to the rise in short-circuit current levels. As fault currents approach equipment ratings, grid operators must either reinforce protection systems or consider alternative solutions to ensure safe and reliable operation. Conventional approaches, such as upgrading switchgear and circuit breakers, often involve significant investment and prolonged downtime. High Temperature Superconductor (HTS) Fault Current Limiters (FCLs) of the saturated-core type offer a promising alternative by reducing fault current levels, thereby limiting the need for costly protection system upgrades or allowing such investments to be deferred. Although HTS-based Superconducting Fault Current Limiters (SFCLs) have been successfully demonstrated, they have not been adopted by utilities, primarily due to high initial investment costs.

In this context, the present study conducts a Techno-Economic Assessment (TEA) of the Saturated Iron Cores Superconducting Fault Current Limiter (SIC-SFCL) to evaluate its feasibility in practical power system environments. A case study in Portugal is presented, analyzing the impact of the integration of a new wind farm into the Portuguese distribution grid, with the objective of determining whether the implementation of a SIC-SFCL is more economically advantageous than upgrading conventional protection equipment (switchgear and circuit breakers).

The economic analysis identifies the conditions under which the SFCL deployment becomes cost-effective, offering valuable insights for utilities and grid operators considering the integration of superconducting technologies. This assessment therefore contributes to overcoming barriers to SFCL deployment and supports the transition towards more resilient and renewable-based power systems.

Keywords: Renewable energy integration, superconducting fault current limiter (SFCL), techno-economic assessment (TEA).

Resumo

A integração de novas fontes de geração renovável, em particular parques eólicos, nas redes elétricas existentes apresenta desafios técnicos significativos devido ao aumento dos níveis de corrente de curto-circuito. À medida que as correntes de defeito se aproximam dos limites nominais dos equipamentos, os operadores de rede têm de reforçar os sistemas de proteção ou considerar soluções alternativas para garantir uma operação segura e fiável. As abordagens convencionais, como a substituição ou o reforço dos dispositivos de proteção da rede, como disjuntores e seccionadores, implicam frequentemente investimentos elevados e longos períodos de indisponibilidade. Os limitadores de corrente supercondutores do tipo núcleos saturados, oferecem uma alternativa promissora ao reduzir os níveis de corrente de defeito, limitando assim a necessidade de dispendiosas modificações dos sistemas de proteção ou permitindo o adiamento desses investimentos. Embora os limitadores de corrente baseados em supercondutores de alta temperatura já tenham sido demonstrados com sucesso, ainda não foram adotados pelas empresas de energia, sobretudo devido aos elevados custos de investimento inicial.

Neste contexto, o presente estudo realiza uma análise tecno-económica do limitador de corrente supercondutor de núcleos saturados, com o objetivo de avaliar a sua viabilidade num contexto real. É apresentado um caso de estudo em Portugal, analisando o impacto da integração de um novo parque eólico na rede de distribuição portuguesa, com o intuito de determinar se a implementação do dispositivo supercondutor é economicamente mais vantajosa do que o reforço dos equipamentos de proteção da rede (disjuntores e seccionadores).

A análise económica identifica as condições em que a implementação do limitador de corrente baseados em supercondutores de alta temperatura se torna economicamente viavel, oferecendo contributos relevantes para as empresas de energia e operadores de rede que considerem a integração de tecnologias supercondutoras. Esta avaliação contribui, assim, para ultrapassar barreiras à adoção dos limitadores de corrente supercondutores e apoia a transição para sistemas elétricos mais resilientes e assentes em energias renováveis.

Palavras-chave: Integração de energias renováveis, limitador de corrente de supercondutor, análise tecno-económica.

Contents

List of Figures x

List of Tables xii

Acronyms xiv

Symbols xvi

1 Introduction 1

1.1 Motivation 1
1.2 Objectives 2
1.3 Organization 2

2 Literature Review 4

2.1 Fault Current in Power Systems 4
2.1.1 Introduction to Fault Currents 4
2.1.2 Methods for Limiting short-circuit Currents 6
2.1.2.1 Conventional Solutions 6
2.1.2.2 Fault Current Limiters 7
2.2 Superconducting Fault Current Limiters 8
2.2.1 Superconductivity 8
2.2.1.1 Fundamentals of Superconductivity 8
2.2.1.2 High temperature superconductors 10
2.2.2 Types of Superconducting fault current limiters 11
2.2.2.1 Resistive type 12
2.2.2.2 Shielded iron core or Transformer type 14
2.2.2.3 Saturated iron Cores type 15
2.2.2.4 Summary 16
2.2.3 State of the art 16

3 Case study: Methodology 20

3.1 Introduction 20
3.2 Impact of Wind Farm Integration into the Distribution Grid 21
3.2.1 Modeling and Steady-State Analysis of the selected power grid . 21
3.2.2 Wind farm integration 24
3.2.3 Wind farm short-circuit current contribution 25
3.3 Techno-Economic Assessment of the SIC-SFCL 26
3.3.1 SIC-SFCL Specifications 27
3.3.2 Inventory analysis 27
3.3.2.1 Iron cores 28
3.3.2.2 DC bias coil 29
3.3.2.3 AC coils 30
3.3.2.4 Cryogenic system 32
3.3.3 Loss Estimation 34
3.3.4 CAPEX and OPEX estimation 36
3.3.5 Economic analysis: Upgrading grid protection vs SIC-SFCL integration 36
3.3.5.1 Investment Requirements for Grid Protection Upgrades 36
3.3.5.2 Evaluation of Economic Performance Indicator 37

4 Case Study: Results analysis **38**
4.1 Analysis of the Impact of Wind Farm Integration into the Distribution Grid 38
4.1.1 Modeling and Steady-State Analysis of the selected power grid . 38
4.1.2 Wind Farm integration 40
4.1.3 Wind farm short-circuit current contribution 41
4.1.3.1 Scenario 1: 37.5 MW wind farm 42
4.1.3.2 Scenario 2: 63 MW wind farm 43
4.2 Techno-Economic Assessment of a SIC-SFCL 46
4.2.1 SIC-SFCL Specifications 46
4.2.2 Inventory analysis 48
4.2.2.1 Iron cores 48
4.2.2.2 DC bias coil 50
4.2.2.3 AC coils 51
4.2.2.4 Cryogenic system 51
4.2.3 Loss estimation 52
4.2.4 CAPEX and OPEX estimation 53
4.2.5 Economic analysis: Upgrading grid protection vs SIC-SFCL integration 54
4.2.5.1 Investment Requirements for Grid Protection Upgrades 54
4.2.5.2 Evaluation of Economic Performance Indicator 54

5 Conclusion and future work **56**

5.1 Final review 56
5.2 Future work 57

Bibliography **58**

Annexes

I Complementary information regarding the methodology **64**

List of Figures

2.1 Types of short circuits. 5
2.2 short-circuit waveform [adapted from [9]] 6
2.3 Locations of FCLs in power systems [14]. 7
2.4 Superconductors characteristics. 9
2.5 T-J-B Diagram [19]. 10
2.6 Magnetic phase diagram for type-I (a) and type-II (b) superconductors. . . . 10
2.7 Chronological discovery of T_c over the years [19]. 11
2.8 SuperPower SCS4050 2G HTS Wire Specification [23] 12
2.9 Classification of SFCL. 12
2.10 Pure Resistive Superconducting Fault Current Limiter (R-SFCL) 13
2.11 Operation of a R-SFCL. 13
2.12 R-SFCL with magnetic field assisted quench. 14
2.13 Shielded Iron Core Superconducting Fault Current Limiter (SC-SFCL). . . . 14
2.14 SIC-SFCL. 15
2.15 Eccoflow prototype [29]. 16
2.16 35 kV SIC-SFCL developed by Innopower. 17
2.17 220 kV SIC-SFCL developed by Innopower. 18

3.1 Flowchart of the presented methodology. 20
3.2 Model of grid under study. 21
3.3 Schematic diagram of the Doubly-Fed Induction Generator (DFIG)-based wind farm integrated in the distribution network. 25
3.4 Schematic diagram of the SIC-SFCL at the grid connection substation. . . . 27
3.5 Design of a single-phase SIC-SFCL. 29

4.1 Simulink model of the grid under study. 39
4.2 Simulink model of the wind farm. 40
4.3 Active and reactive power generated by the wind farm. 41
4.4 Current at the Varosa substation under a fault event without wind farm integration. 42

4.5 Active power generated by the 37.5 MW wind farm. 42
4.6 Current contribution from the 37.5 MW wind farm at the Varosa substation during the fault. 43
4.7 Current at the Varosa substation during a fault event with the integration of a 37.5 MW wind farm. 44
4.8 Active power generated by the 63 MW wind farm. 44
4.9 Current contribution from the 63 MW wind farm at the Varosa substation during the fault. 45
4.10 Current at the Varosa substation during the fault. 45
4.11 Current at the 30 kV busbar under a fault event at the Varosa busbar. 46
4.12 Current at the 30 kV busbar under a fault at the grid connection substation. 47
4.13 Top view of the SIC-SFCL. 48

List of Tables

2.1 Comparative of the characteristics of the main types of SFCL [11, 27] 16
2.2 Main specifications of the R-SFCL developed in the Eccoflow project [28]. . 17
2.3 Main specifications of the two prototypes developed by Innopower. 18
2.4 Summary of some SFCL projects. 19

3.1 Busbars of the grid model. 22
3.2 Parameters of the iron cores. 29
3.3 Parameters of the Direct Current (DC) bias coil. 31
3.4 Parameters of the Alternating Current (AC) coils. 32
3.5 Parameters of the cryostat. 33
3.6 Parameters of the current leads. 33
3.7 Parameters of the cryocooler. 34

4.1 Parameters of the Valdigem's power transformer. 38
4.2 Results of the load flow analysis. 40
4.3 General specifications of the SIC-SFCL. 47
4.4 Parameters of the iron cores. 49
4.5 Parameters of the DC bias coil. 50
4.6 Parameters of the AC coils. 51
4.7 Parameters of the dewar. 52
4.8 Losses of the SIC-SFCL. 53
4.9 Capital Expenditure (CAPEX) of the SIC-SFCL. 53
4.10 Operational Expenditure (OPEX) of the SIC-SFCL. 53
4.11 Sensitivity analysis 55

I.1 Characteristics of the Varosa substation (adapted from [40]). 64
I.2 Transformers at the Valdigem's substation (adapted from [41]). 64
I.3 Transmission lines of the grid under study (adapted from [40]). 65
I.4 Cable characteristics (adapted from [42, 43]). 65
I.5 Loads of the grid's model 66

I.6 Standard characteristics of 60/30 kV power transformers used by E-REDES (adapted from [67]). 66
I.7 Main specifications of the DFIG 67

Acronyms

1G	Superconducting material of first generation
2G	Superconducting material of second generation
AC	Alternating Current
ACSR	Aluminum Conductor Steel Reinforced
Bi-2212	$Bi_2Sr_2CaCu_2O_{8+x}$
Bi-2223	$(Bi, Pb)_2Sr_2Ca_2Cu_3O_{10-x}$
BSCCO	Bismuth Strontium Calcium Copper Oxide
CAPEX	Capital Expenditure
DC	Direct Current
DFIG	Doubly-Fed Induction Generator
EDP	Energias de Portugal
FCL	Fault Current Limiter
FEM	Finite Elements Method
HTS	High Temperature Superconductor
IEA	International Energy Agency
LCC	Life-cycle cost
mmf	Magnetomotive Force
OPEX	Operational Expenditure

R-SFCL	Resistive Superconducting Fault Current Limiter
REBCO	Alloy of rare-earth element with barium-copper-oxide
REN	Rede Energia Nacional
RES	Renewable Energy Sources
RMS	Root Mean Square
SC-SFCL	Shielded Iron Core Superconducting Fault Current Limiter
SFCL	Superconducting Fault Current Limiter
SIC-SFCL	Saturated Iron Cores Superconducting Fault Current Limiter
SS	Switching Stations
TEA	Techno-Economic Assessment
YBCO	Yttrium Barium Copper Oxide

Symbols

A_{in}	Inner surface area of the cryostat (m^2)
A_{out}	Outer surface area of the cryostat (m^2)
B	Magnetic flux density (T)
B_c	Critical magnetic flux density (T)
C	Capacitance (F)
$c_{cryocooler}$	Cost of the cryocooler (€)
C_t	Costs in year t
$d_{AC,avg}$	Average diameter of each AC coil (m)
$d_{pancake,avg}$	Average diameter of each pancake in the DC bias coil (m)
δ	Thickness of the vacuum insulation layer (m)
ΔT	Temperature difference across the insulation layers (K)
ρ_{core}	Density of the iron cores material (kg/m^3)
d_{inAC}	AC coils inner diameter (m)
d_{inDC}	Pancake inner diameter (m)
d_{outAC}	AC coils outer diameter (m)
d_{outDC}	Pancake outer diameter (m)
f	Frequency (Hz)
$f_{pancake}$	Pancake factor
G	Conductance (S)
H	Magnetic field (A/m)
H_c	Critical magnetic field (A/m)
H_{c1}	Lower critical magnetic field (A/m)
H_{c2}	Upper critical magnetic field (A/m)

h_{cores}	Height of the iron core (m)
H_t	Time horizon
I_c	Critical current (A)
I_{DC}	DC bias current (A)
I_n	Nominal current (A)
I_p	Peak short-circuit current (A)
I_r	Rated current (A)
I_{sc}	Short-circuit current (A)
I_k	Steady-state RMS short-circuit current (A)
I_k''	Subtransient RMS short-circuit current (A)
I_k'	Transient RMS short-circuit current (A)
J_c	Critical current density (A/m^2)
k	Stacking factor
L	Inductance (H)
L_1	Coil 1
L_2	Coil 2
$l_{conductor}$	Total conductor length (m)
l_{HTS}	Total tape length (m)
λ	Apparent thermal conductivity ($W/m \cdot K$)
LN_2	Liquid nitrogen
L_0	Lorenz number ($2.45 \times 10^{-8}\,\mathrm{W\,\Omega\,K^{-2}}$)
L_{Shunt}	Shunt coil
m_{cores}	Total mass of the cores (kg)
η	Efficiency of the cryocooler (%)
n_{cores}	Number of cores
$n_{pancakes}$	Number of pancakes of the DC bias coil
n_{turns}	Turns per pancake of DC bias coil
$n_{turnsAC}$	Turns per coil AC
P	Active power (W)
P_{core}	Core losses (W/kg)
P_{cores}	Iron Cores losses (W)
P_{eddy}	Eddy current losses (W)
P_{el}	Electrical power consumption of the cryocooler (W)

P_{hyst}	Hysteresis losses (W)
P_{jAC}	Joule losses in the AC coil (W)
P_{turnAC}	Perimeter of a single turn in the AC coil (m)
P_{turnDC}	Perimeter of a single turn in the DC bias coil (m)
P_{th}	Cooling capacity (W)
P_{wf}	Active power generated by the wind farm (W)
Q	Reactive power (Var)
Q_{cl}	Heat input of the current leads (W/kA)
R	Resistance (Ω)
r	Discount rate
$\rho_{conductor}$	Resistivity of the conductor ($\Omega \cdot m$)
R_{Shunt}	Shunt Resistance (Ω)
S	Apparent power (VA)
S_{ac}	Cross-sectional area of the AC column (m^2)
$S_{conductor}$	Cross-sectional area of the conductor (m^2)
S_{dc}	Cross-sectional area of the DC column (m^2)
S_{new}	New base power (VA)
S_{old}	Old base power (VA)
S_{sc}	Short-circuit capacity (VA)
S_{yoke}	Cross-sectional area of the yoke (m^2)
T	Temperature (K)
T_C	Temperature of the cold end of the current lead (K)
T_c	Critical Temperature (K)
T_H	Temperature of the warm end of the current lead (K)
T_l	Lifetime
V	Voltage (V)
V_{cores}	Volume of the iron cores (m^3)
V_n	Nominal voltage (V)
w	Inner window width of the iron core (m)
W_{cores}	Weight of the iron cores (kg)
X	Reactance (Ω)
X_c	Capacitive reactance (Ω)

Y	Admittance (S)
Y_{eq}	Equivalent admittance (S)
Y_{new}	Admittance under the new base power (S)
Y_{old}	Admittance under the old base power (S)
Z	Impedance (Ω)
Z_{eq}	Equivalent impedance (Ω)
Z_{new}	Impedance under the new base power (Ω)
Z_{old}	Impedance under the old base power (Ω)

1

Introduction

1.1 Motivation

Present and future generations will witness a profound transformation of electric power systems as energy demand continues to rise. The International Energy Agency (IEA) projects a rise in global electricity demand by approximately 3.3% in 2025 and 3.7% in 2026 [1]. The same global pattern is also reflected in Portugal, where Rede Energia Nacional (REN), the Portuguese transmission system operator, reported that electricity consumption increased by 3.8% between July 2024 and July 2025, and by 2.4% from January to July 2025 compared to the same period in the previous year [2].

As a result of growing electricity demand, the integration of distributed generation has been growing at a very high rate. On a global level, the use of the renewable energy sources already accounted for an estimated 32% of the global total generation by 2024, and it continues to rise [3]. Within this transition, solar PV and wind energy have emerged as the leading technologies, with a combined contribution projected to increase from 15% in 2024 to 17% in 2025, and to surpass 19% by 2026 [1]. For example, Energias de Portugal (EDP) established its 2023-2026 strategic plan to add 4.5 GW of renewable capacity annually—97% of which corresponds to solar PV and wind—totaling approximately 18 GW in increments by 2026. This expansion is expected to raise its overall installed renewable capacity to 33 GW in 2026, with a longer-term objective of achieving 50 GW by 2030 [4].

This increasing integration of Renewable Energy Sources (RES) has contributed, and will contribute in the future, to even more overloaded power systems [5]. All these new generation systems added to the existing power systems have led to a huge rise in fault current levels, bringing severe consequences for the stability, and security of power systems, since current levels may exceed the limits of the installed protection device (circuit breakers). For example, in the Shanghai municipal area, over half of its eight 500 kV substations are currently experiencing a scenario where short-circuit current levels are nearing 63 kA [6].

To address these problems, conventional solutions such as upgrading switchgear, splitting busbars, or installing current-limiting reactors have been adopted, though they are often costly and not technically feasible. An alternative is the use of superconducting materials, which intrinsically act as fault current limiters due to their natural physical properties. This characteristic has driven the development of superconducting-based current-limiting solutions, such as Superconducting Fault Current Limiters (SFCLs), which have already been tested in real power grids, demonstrating a highly satisfactory performance.

The emerging market for superconducting devices, particularly fault current limiters, still faces significant barriers, mainly related to design and manufacturing costs. However, the continuous decrease of the superconductor materials combined with the need for high reliable solutions, may encourage utilities and grid operators to consider the integration of these superconducting devices.

1.2 Objectives

The main objectives of this thesis are:

- Development of a methodology to conduct a Techno-Economic Assessment (TEA) of the Saturated Iron Cores Superconducting Fault Current Limiter (SIC-SFCL), aimed at serving as a reference tool for future studies and designs of the device, while supporting the estimation of both capital and operational costs.
- Demonstrate that the integration of a SIC-SFCL represents a more technically and economically viable solution compared to upgrading the breaking capacity of existing protection devices in the power grid.
- Demonstrate to utilities and grid operators the technical and economic benefits of integrating SFCLs into modern power grids.

1.3 Organization

This document is structured into four chapters:

- **Chapter 1 -** Introduction

  In this chapter, a brief overview and framework of the subject under study are presented, including its motivation and the goals to be accomplished.

- **Chapter 2 -** Literature Review

  This chapter establishes the contextual foundation for understanding SFCLs. It begins by discussing the phenomenon of fault currents in power systems, their causes, consequences, and methods to mitigate high fault currents, highlighting the advantages of superconducting over conventional solutions. To introduce the SFCLs a brief overview on superconductivity, High Temperature Superconductors (HTSs) and the main types of SFCLs is conducted. Last but not least, the state fo the art of the SFCL highlights recent advancements, practical implementations, and ongoing research challenges related to these superconducting devices.

- **Chapter 3 -** Case study: Methodology

  This chapter presents the methodology adopted in this case study. It begins with an analysis of the impact of integrating a wind farm into the distribution network, describing the approach used to evaluate its technical implications. Subsequently, a methodology for conducting a TEA of a SIC-SFCL is developed, focusing on both capital and operational expenses.

- **Chapter 4 -** Case study: Results analysis

  This chapter presents and analyzes the results obtained from the case study, following the methodology mentioned in the chapter 3. In the end, the economic analysis of both considered solutions is compared and discussed, regarding its cost-effectiveness.

- **Chapter 5 -** Conclusion

  In this chapter, a final review of the results obtained throughout the study is presented, along with suggestions for future works.

2

Literature Review

2.1 Fault Current in Power Systems

2.1.1 Introduction to Fault Currents

Electric power transmission and distribution systems play a crucial role in delivering reliable energy to meet the growing demands of our modern society. However, these systems are susceptible to faults caused by natural forces (falling trees, birds, lightning strikes) or aged or accidentally damaged insulation, leading to a sudden reduction in the power grid's impedance causing a short circuit. The consequences of these short-circuit events can be severe, not only for the equipment conditions but also for human lives. This happens because the current generated due to a short-circuit I_{sc} can be 100 times greater than the nominal current I_n of the system, leading to high mechanical and thermal stresses, which are propositional to I_{sc}^2 [7]. The main consequences associated with the occurrence of short-circuit events in power systems are summarized as follows:[8, 9]:

- Permanent damage to generators, busbars and transformers;
- Overheating, causing permanent damage to protection equipment (circuit-breakers) and the deformation of conductors;
- Fire and danger to life;
- Voltage dips;
- Power outages.

Short circuits are classified in two categories: symmetrical or asymmetrical.

Symmetrical faults occur when all three phases of the system are simultaneously affected, whereas asymmetrical faults involve only one or two phases. Asymmetrical faults can be phase-to-ground, phase-to-phase, or double-phase-to-ground.

Figure 2.1 illustrates the five different types of short circuits.

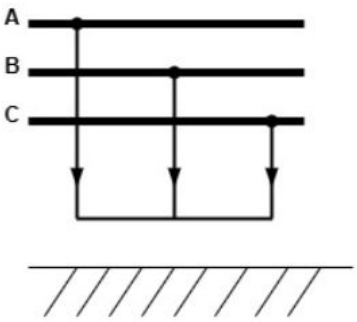

(a) Three-phase short circuit

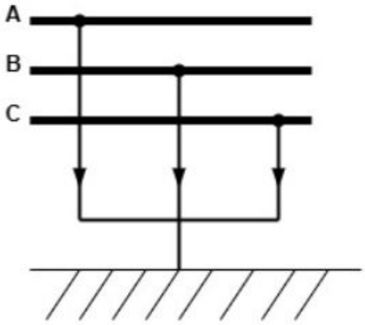

(b) Three-phase-to-ground short circuit

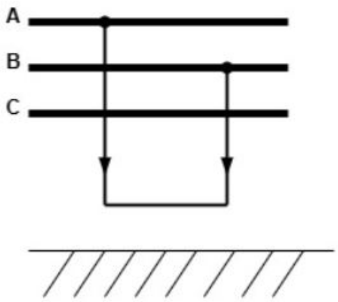

(c) Phase-to-phase short circuit

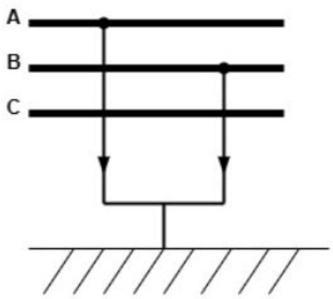

(d) Phase-to-phase-to-ground short circuit

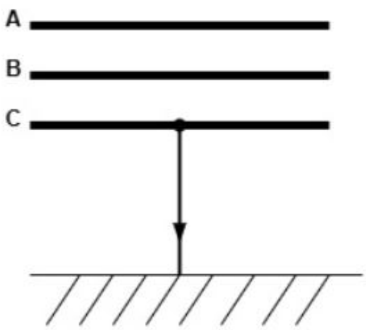

(e) Phase-to-ground short circuit

Figure 2.1: Types of short circuits.

A general short-circuit current waveform is shown in Figure 2.2. In addition to the Alternating Current (AC) component, a short-circuit also contains a Direct Current (DC) component. The presence of this DC component causes the current to exhibit asymmetric characteristics in the moments immediately following the fault. As illustrated, a short-circuit can be divided into three characteristic periods: subtransient, transient, and steady-state. These periods are associated with the variation of the generator's reactance during the fault. Consequently, different reactance values result in different short-circuit currents: I_k'' denotes the subtransient Root Mean Square (RMS) short-circuit current, I_k' the

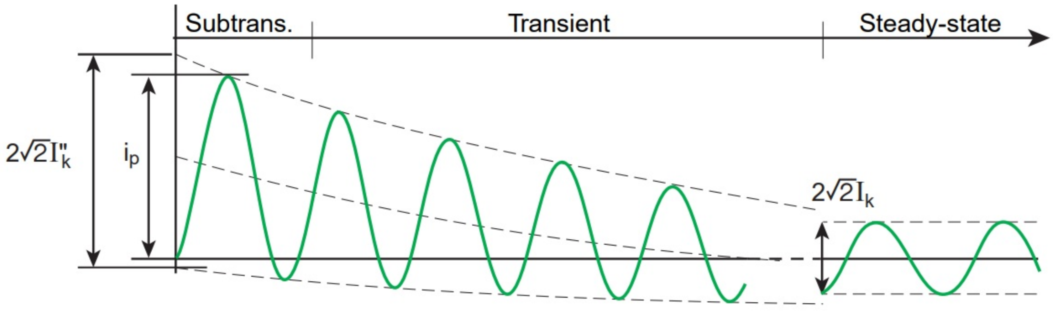

Figure 2.2: short-circuit waveform [adapted from [9]]

transient RMS short-circuit current, and I_k the steady-state RMS short-circuit current. The maximum instantaneous value of the short-circuit current is represented by I_p, the peak short-circuit current [9].

2.1.2 Methods for Limiting short-circuit Currents

2.1.2.1 Conventional Solutions

Nowadays, there are some conventional solutions to cope with fault currents distribution and transmission networks. These measures include [10, 11]:

- Busbar splitting.
- High impedance transformers and current limiting air core reactors.
- Circuit-breaker upgrades.
- High-voltage current limiting fuses.
- I_s-Limiters.
- Construction of new substations.

Although these measures can be effective in protecting the grid and reducing the impact of short-circuit currents, some of them could be very expensive and compromise the power system's stability and reliability.

For instance, measures like busbar splitting, selecting higher-impedance transformers, or installing current-limiting air-core reactors, add permanent impedance in both fault and nominal conditions, increasing voltage drop and power losses.

Other solutions like fuses or explosive devices like the Is-limiter, present small impedance at nominal load and a fast increase of impedance at fault. However, they need to be replaced after each fault.

Alternatively, upgrading circuit breakers to higher breaking capacities—or, in the extreme, constructing new substations - are just too expensive.

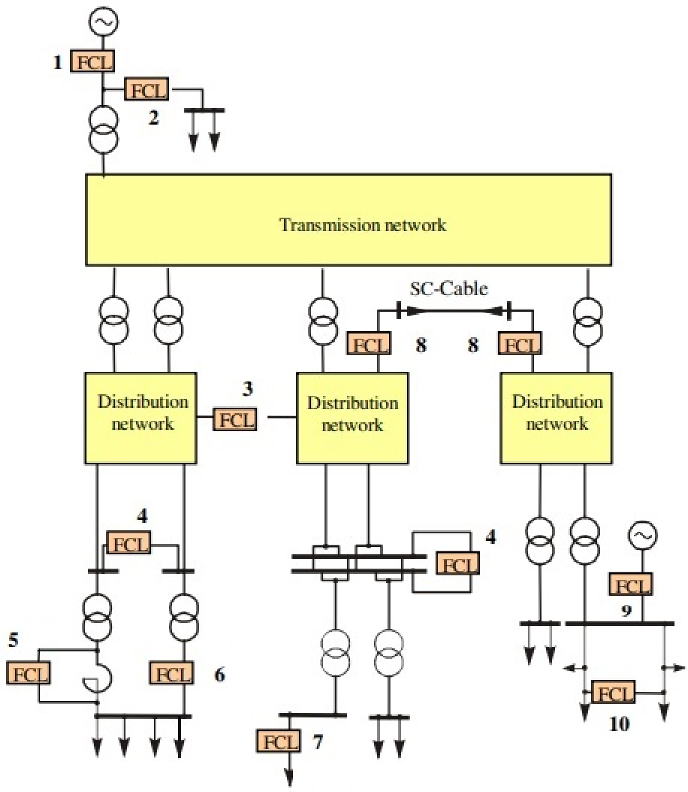

Figure 2.3: Locations of FCLs in power systems [14].

2.1.2.2 Fault Current Limiters

Due to the increasing demand for higher power quality, the most desirable solution to deal with short circuits is to limit the high fault currents. A Fault Current Limiter (FCL) does not aim to completely eliminate the fault current; instead, its purpose is to decrease the fault current to a level that can be managed by existing equipment and devices.

The successful installation of FCLs on the power grid will not only avoid the use of conventional solutions that are not reliable and can be very expensive but also avoid equipment damage and replacement (e.g. circuit-breakers), and enhance the grid stability [12].

Figure 2.3 illustrates potential applications of FCLs within the transmission and distribution network. These include [13]:

1. Generator connection;
2. Power station auxiliaries;
3. Network coupling;
4. Busbar coupling;
5. Shunting current limiting reactors;
6. Transformer feeder;
7. Busbar connection;
8. Combination with other technologies (for example superconducting cables);
9. Coupling local generating units;
10. Closing ring circuits.

In order to be effectively integrated into modern power systems, a FCL must satisfy a set of technical and operational requirements. These requirements ensure that the device not only limits fault currents to acceptable levels but also operates reliably under normal system conditions without compromising stability, efficiency, or protection coordination. Therefore, it is essential for a FCL to meet the following requirements [6, 11, 15]:

- Negligible impedance at normal conditions;
- Fast increase of impedance at fault condition;
- Rapid detection and initiation of limiting action;
- Fast and automatic recovery to normal operation after the clearing of a fault;
- Capability to intercept and handle a series of faults in a short period;
- Compatibility with the already existing protection systems of the grid;
- High reliability;
- Low maintenance costs.
- Low AC loss and voltage drop.

2.2 Superconducting Fault Current Limiters

2.2.1 Superconductivity

2.2.1.1 Fundamentals of Superconductivity

The discovery of the phenomenon of superconductivity took place in 1911, when the Dutch physicist Heike Kamerlingh Onnes, following his success in liquefying helium 3 years earlier [16], was researching about the resistivity of metals at low temperatures. Onnes observed, as illustrated in Figure 2.4a, that the resistivity of the mercury abruptly disappeared when the temperature reached 4.2K (liquid helium). This observation made Onnes conclude that below a certain critical temperature T_c, some materials lose their resistivity. This was a huge discovery since until then, it was only known that the resistance of metals decreased with temperature. Illustrated in Figure 2.4b, the contrast between the loss of resistivity with decreasing temperature T in normal conductors and superconductors is remarkable.

Although resistivity loss is a defining characteristic of superconductors, it is not sufficient to fully define superconductivity. Heike Kammerlingh Onnes discovered that a superconductor could lose its superconducting state when exposed to a certain value of a magnetic field. This means that the superconducting state cannot be maintained in the presence of a magnetic flux exceeding the critical value B_c, even when the temperature is lower than the critical temperature T_c.

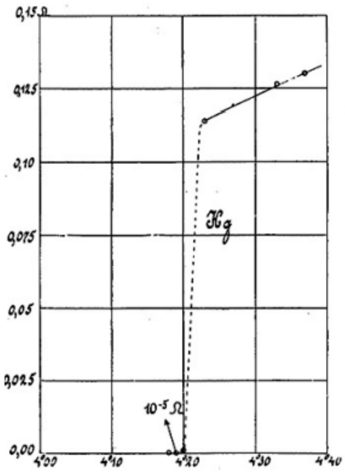

(a) Resistivity of mercury as a function of temperature [17].

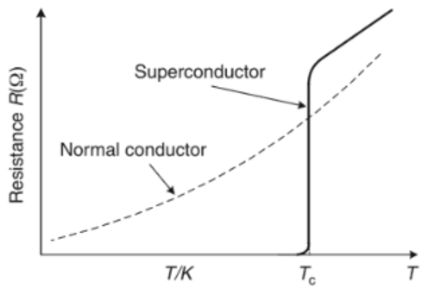

(b) Superconductor vs normal conductor resistance

Figure 2.4: Superconductors characteristics.

In 1933, German physicists Walther Meissner and Robert Ochsenfeld studied the interaction between superconductors and magnetic fields and discovered that superconductors change from a non-superconducting (normal) to a superconducting state in the presence of a magnetic flux. When subjecting a superconducting material (with $T < T_c$) to a magnetic flux density B, where $B < B_c$, the magnetic flux inside is completely excluded from the material, and the inner magnetic field is null ($B = 0$). On the other hand, when in a non-superconducting state, the material is fully penetrated by the magnetic flux, thus $B \neq 0$. This phenomenon was later called the Meissner effect and shows that superconductors are perfect diamagnets [18].

While superconducting materials have the remarkable ability to carry electrical current without resistance, this capacity is not limitless. A superconductor's capability to transport current is constrained, and it loses its superconducting state when the transported current exceeds a specific value known as the critical current I_c. Hence, there is a limit to the current density, referred to as the critical current density J_c, which marks the boundary between the superconducting and normal states.

Thus, superconductivity is defined by three non-independent parameters, T_c, B_c and J_c. These critical parameters can be related through the T-B-J diagram, as shown in Figure 2.5. The material is in the superconductor state if its volume is within these limits.

The superconductors are classified into two types: Type I and Type II superconductors.

Type I superconductors have only one critical magnetic field H_c, turning to the normal state whenever $H > H_c$ (Figure 2.6a).

On the other hand, Type II superconductors have two critical magnetic fields: the lower critical field H_{c1} and the upper critical field H_{c2} (Figure 2.6b).

Unlike type I superconductors, when the external magnetic field H satisfies $H_{c1} < H < H_{c2}$, the type II superconductor does not change from the superconducting state to

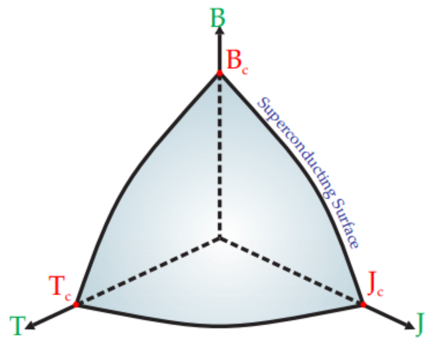

Figure 2.5: T-J-B Diagram [19].

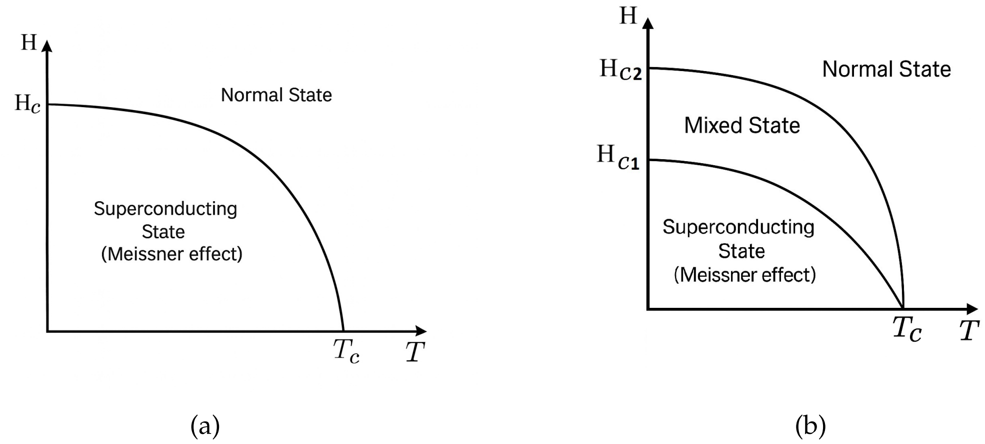

Figure 2.6: Magnetic phase diagram for type-I (a) and type-II (b) superconductors.

the normal state. Conversely, it changes to a new state called mixed state. The mixed state is a mixture of both normal and superconducting states, where they both coexist. In this state, the Meissner effect is no longer applicable, which means there is no perfect diamagnetism, and the resistivity is not null, resulting in AC losses. When $H > H_{c2}$ the flux fully penetrates the superconductor material, so it returns to the normal state.

2.2.1.2 High temperature superconductors

Until 1986, it was thought that the critical temperature limit of the superconductor materials was around 25K. Everything changed when George Bednorz and Alexander Müller observed critical temperatures around 30K in the ceramic compound of BaLaCuO [20]. This revolutionary discovery set a huge quest for superconducting materials with even higher critical temperatures (see Figure 2.7). Until the end of the 20th century, many other HTS have been found, mostly based on the copper-oxide compound (cuprates), such as Bismuth Strontium Calcium Copper Oxide (BSCCO) and Yttrium Barium Copper Oxide (YBCO). With the capability for operation in liquid nitrogen (77 K), both BSCCO and YBCO are perfectly suited for engineering applications, eliminating the necessity for expensive cryogenic systems relying on liquid helium, since nitrogen is much cheaper than helium.

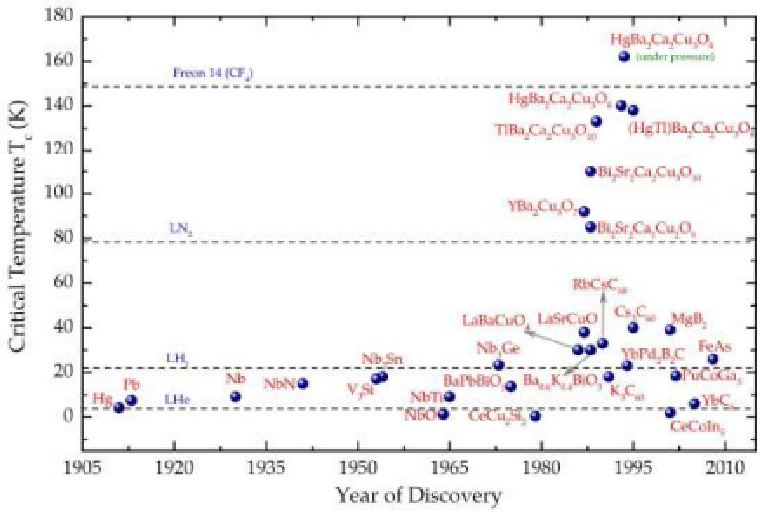

Figure 2.7: Chronological discovery of T_c over the years [19].

The first High Temperature Superconductor (HTS) material were commercialized in bulks, which can be single crystal or polycrystalline.

Currently, HTS are predominantly commercialized in tapes, developed and optimized to be flexible and carry as much current as possible.

HTS tapes are classified into two categories:

- 1G tapes - use BSCCO filaments embedded in a silver matrix, which provides mechanical robustness and some flexibility. Two different variations of BSCCO are considered for the manufacture of 1G tapes. The Bi-2223 has a higher critical temperature (110 K) than Bi-2212 (90 K) as well as higher critical current density and Bi-2212 has less degradation of its properties in the presence of magnetic field [21].

- 2G tapes - usually called coated conductors and typically based on REBCO, like YBCO, which are produced by a multilayer thin-film process, as shown in Figure 2.8. This design delivers better performance at higher temperatures, greater mechanical robustness, higher critical current density and lower AC losses, compared to 1G tapes [22].

2.2.2 Types of Superconducting fault current limiters

Superconducting Fault Current Limiters (SFCLs) are generally classified into two main categories: resistive and inductive. The main types within each category are summarized in Figure 2.9.

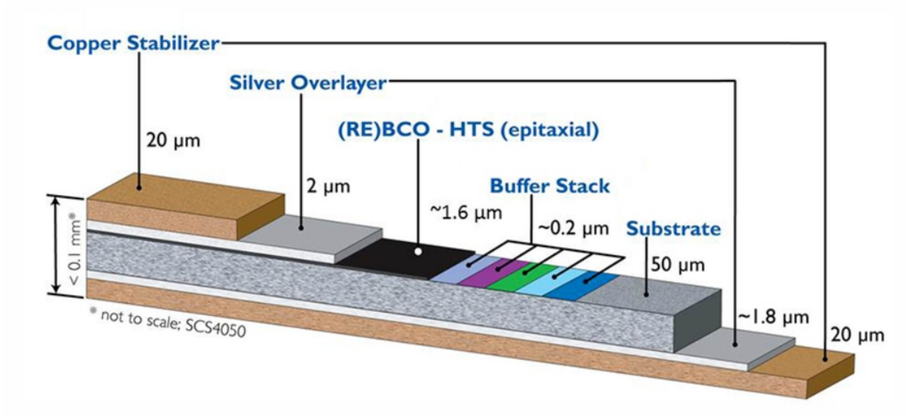

Figure 2.8: SuperPower SCS4050 2G HTS Wire Specification [23]

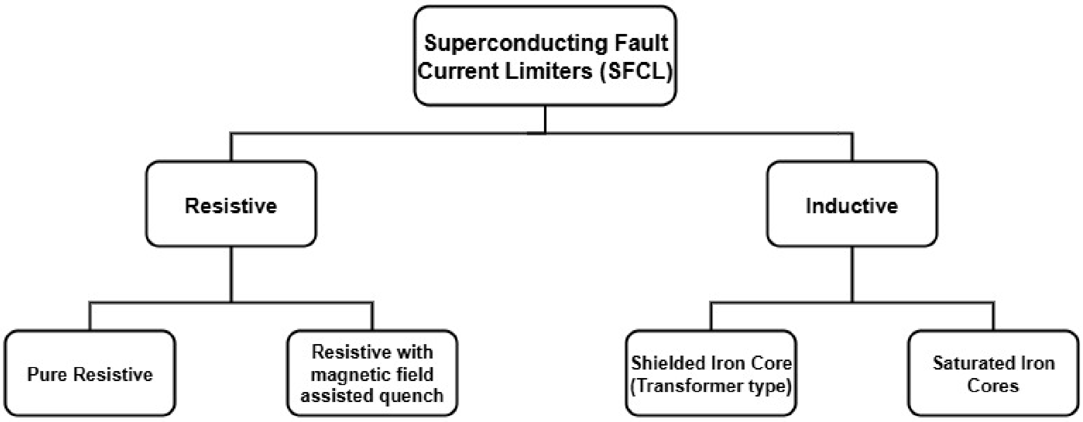

Figure 2.9: Classification of SFCL.

2.2.2.1 Resistive type

Pure resistive

The pure Resistive Superconducting Fault Current Limiter (R-SFCL) [6, 11] is the most straightforward type of SFCL since it uses the natural properties of superconducting materials to limit the fault current.

Under normal operating conditions, the resistance of the superconductor is negligible. However, when a fault occurs and the short-circuit current exceeds the I_c, the superconducting material transitions from the superconducting state to the normal resistive state (quench).

The extended length of HTS material means that not all parts of the material transit simultaneously from the superconducting state to the normal state, resulting in *hot-spots*. A hot-spot is essentially the occurrence of one region overheating more than another. The existence of hot-spots can result in damage, or even, the destruction of the superconducting material and the device. To prevent the occurrence of hot spots, a shunt R_{Shunt} is added all over the length of the HTS material. A shunt is nothing more than a resistance in parallel with the HTS material (see Figure 2.10), which works as an alternative path for the current to flow during the fault. Furthermore, this parallel resistance adjusts the limited current and avoids overvoltages that could occur if the resistance of the HTS material rises too rapidly.

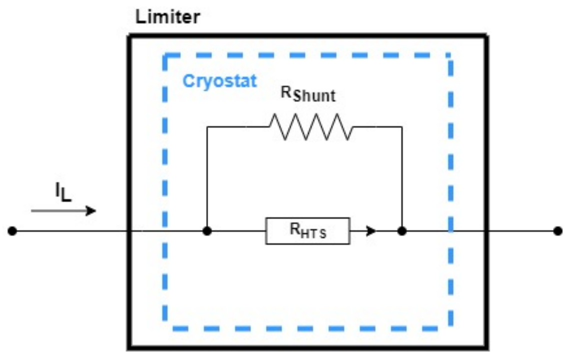

Figure 2.10: Pure R-SFCL .

After the quench and the heating of the superconductor, a recovery time is needed before the SFCL can operate in the normal state again. Typically, the recovery time is at least several seconds, being too long to be accepted by utility standards.

Figure 2.11 shows the operation principle of the R-SFCL.

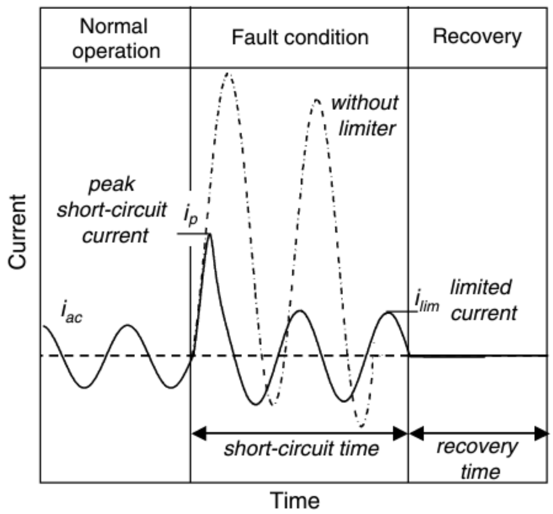

Figure 2.11: Operation of a R-SFCL.

Resistive with magnetic field assisted quench

Another solution was found to solve the inhomogeneity quench problem and the resulting occurrence of hot-spots. Instead of a shunt resistance, a normal conducting coil is added in parallel with the superconductor material (see Figure 2.12). This design uses the magnetic field dependency of the superconductor's critical current. The quench initiates at the superconductor's most vulnerable point, and the increasing resistance of the superconductor forces the current to flow through the parallel coil. The magnetic field

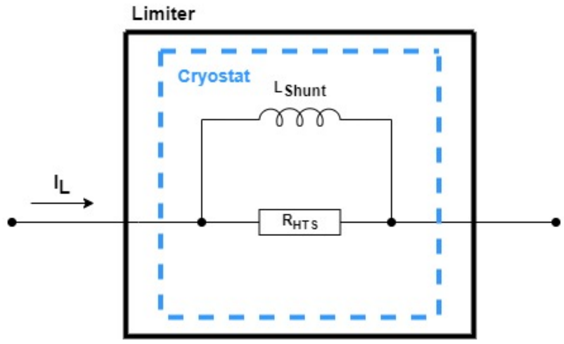

Figure 2.12: R-SFCL with magnetic field assisted quench.

generated by the coil L_{Shunt} reduces the critical current density in the still superconducting segments, accelerating the quench and consequently mitigating the hot-spot issue [11].

2.2.2.2 Shielded iron core or Transformer type

The Shielded Iron Core Superconducting Fault Current Limiter (SC-SFCL) [11] consists of a copper primary winding connected in series with the grid, and a short-circuited secondary winding composed by a HTS cylinder, as shown in Figure 2.13.

In normal operational conditions, the induced current in the superconducting cylinder remains below the I_c, ensuring effective magnetic flux shielding by the superconductor, and preventing its penetration into the iron. Thus, keeping the impedance low.

In the event of a fault, the HTS material of the cylinder loses its superconductivity (quench) due to the increased induced current within the superconducting cylinder, which surpasses I_c. After breaking the HTS shield, it penetrates the iron core, increasing the impedance seen from the primary side of the transformer, and limiting the fault current. This impedance results from the parallel between the resistance of the HTS material and the magnetizing inductance L of the iron core.

Conversely to the R-SFCL, the HTS material is not in series connection with the system to be protected. Therefore, there are no current leads to cryogenic temperatures. However, compared to the R-SFCL it exhibits a significantly larger size and weight, which is a huge disadvantage for this type of FCL. Due to the quench, a recovery time of a few seconds is needed.

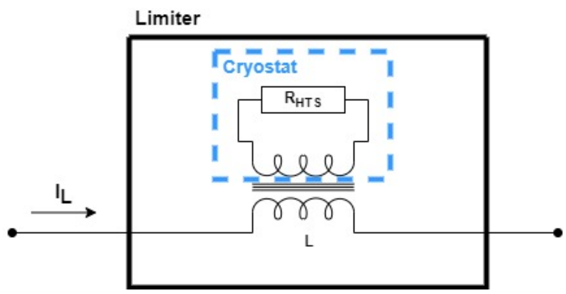

Figure 2.13: SC-SFCL.

2.2.2.3 Saturated iron Cores type

The Saturated Iron Cores Superconducting Fault Current Limiter (SIC-SFCL) [11, 24, 25], also known as DC-biased cores SFCL, consist of two magnetic iron cores embraced by an HTS bias coil (DC) and two AC copper-made coils wrapped around the iron cores. The DC coil is supplied by an independent source to drive the cores into deep saturation in normal operation, while the two AC coils are connected in series with the power grid under protection, and with opposite winding directions so that the flux generated by the DC coil (in L_1 and L_2) has different directions (see Figure 2.14).

Under normal conditions, the DC currents produced by the superconducting DC coil generate a large DC bias magnetic field, which will drive both iron cores into saturation with low permeability. Since inductance is proportional to the permeability, both inductances of L_1 and L_2 are very small, resulting in a very low impedance.

When the fault occurs, the increasing AC current in the winding will alternately drive the two coils out of saturation and into the region of high permeability. Therefore, the inductances of L_1 and L_2 will increase, limiting the current through an inductive voltage drop at the SFCL terminals (increase of the grid's impedance).

As there is no quench, no recovery time is required, and the SFCL returns to normal operational conditions instantaneously. Moreover, because the HTS material in the DC bias coil is powered by a DC current source and is not connected to the AC circuit, the amount of superconducting material required is reduced, and a smaller cryogenic system is sufficient to remove the low cryogenic losses [11].

Although, in principle, this type of SFCL could be implemented using conventional conductors, the substantial current required to saturate the two cores while maintaining acceptable losses can only be effectively managed with superconducting windings. Therefore, it is the HTS that truly enables this technology [26].

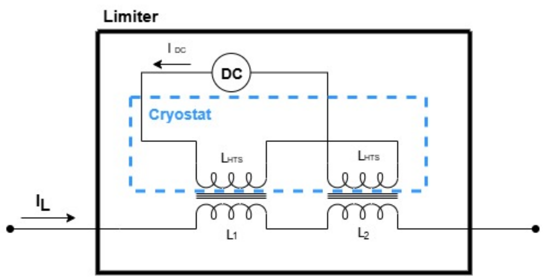

Figure 2.14: SIC-SFCL.

Table 2.1: Comparative of the characteristics of the main types of SFCL [11, 27]
.

	R-SFCL	SC-SFCL	SIC-SFCL
Losses	AC losses and Current Leads	AC losses	Current Leads
Fail Safe	Yes	Yes	Yes
Quench	Yes	Yes	No
Recovery time	Few seconds to minutes	Few seconds	Immediate
Size	Small	Medium to high	High
Voltage drop	Low	Low	Medium
Maintenance cost	Medium	Medium	Low

2.2.2.4 Summary

A brief summary of the advantages and drawbacks of the main types of SFCL is given in Table 2.1.

2.2.3 State of the art

In recent years, several SFCL projects have been developed worldwide. In this section, some of the most notable initiatives are presented and briefly described.

Eccoflow

The Eccoflow project was an European research initiative focused on developing a SFCL for a medium-voltage network. The prototype (shown in Figure 2.15) developed in this project was a three-phase 24 kV/1 kA R-SFCL based on 2G tape made of YBCO. The device was successfully installed and tested in Palma de Mallorca (Spain) in 2013. Table 2.2 shows the main specifications of the R-SFCL developed in the Eccoflow project [28].

Figure 2.15: Eccoflow prototype [29].

Table 2.2: Main specifications of the R-SFCL developed in the Eccoflow project [28].

Rated Voltage (kV)	24
Rated Current(kV)	1
Max. Limited Current (kA)	10.8
Recovery Time (s)	<30
Limitation Time (s)	1

ABB

In 1996, ABB developed a three-phase SC-SFCL prototype rated at 10.5 kV and 70 A, with a total power capacity of 1.2 MVA. The three-phase device used bulk Bi-2212 rings as a superconducting element, with each phase containing a tube composed of 16 rings. The prototype was installed at the Kraftwerk am Lontsch hydropower plant in Switzerland. Over the course of a one-year trial, the system experienced no fault events [30].

Innopower

Innopower developed two SIC-SFCL. The first SIC-SFCL developed by Innopower was a three-phase 35 kV/90 MVA SIC-SFCL (see figure 2.16). The device was installed in a transmission network at Puji Station of China Southern Power Grid in January 2008. Its DC bias coil was manufactured using Bi-2223 tape, wound into 44 pancake coils, and the overall structure of the device adopted a hexagonal configuration [31].

(a) Prototype [31].

(b) Photograph of the installation of the SIC-SFCL at Puji Substation [32]

Figure 2.16: 35 kV SIC-SFCL developed by Innopower.

The successful performance of this prototype motivated Innopower to design a second, larger device rated at 220 kV / 300 MVA (see Figure 2.17). The device was installed at Shigezhung substation of the State Grid in Tianjin at the end of 2011, following the same structural configuration as the first. Its DC bias coil was also fabricated from Bi-2223 tape, but in this case wound into 45 pancakes [33].

(a) Prototype [33]

(b) Photograph of the installation of the SIC-SFCL at Shigezhuang substation of Tiang, China [34]

Figure 2.17: 220 kV SIC-SFCL developed by Innopower.

The main characteristics of both prototypes developed by Innopower are summarized in Table 2.3.

Table 2.3: Main specifications of the two prototypes developed by Innopower.

	35 kV/90 MVA	**220 kV/300 MVA**
Rated Voltage (kV)	35	220
Rated Current (kA)	1.5	0.8
Max. Prospective Current (kA)	41	50
Max. Limited Current (kA)	25	30
Max. Line Voltage Drop (%)	<1	<1.25
Reaction Time (ms)	<5	0
Recovery Time (ms)	<800	<500

Table 2.4: Summary of some SFCL projects.

Project	Country/Year	SFCL Type	HTS Material	Specifications
Curl 10 [35]	Germany/2004	R-SFCL	Bi-2212 Bulk	10 kV / 600 A
SuperOx [36]	Russia/2021	R-SFCL	YBCO tape	220 kV / 1.2 kA
Warsaw Elect. Inst [37]	Poland/2016	SC-SFCL	YBCO tape	15 kV / 140 A
T. Ma & C. Liang [38, 39]	China/2018	SIC-FCL	Bi-2223 & YBCO tapes	500 kV / 3.15 kA

Table 2.4 highlights other SFCL projects that have been developed in last years.

3

Case study: Methodology

3.1 Introduction

This work aims to perform a Techno-Economic Assessment (TEA) of the integration of a Saturated Iron Cores Superconducting Fault Current Limiter (SIC-SFCL) into the power system, considering the integration of a wind farm to the Portuguese distribution network.

The methodology starts with an analysis of the impact of wind farm integration on the distribution grid. This begins by defining the network model for simulation and specifying the characteristics of the wind farm. A short-circuit analysis is then performed, first with no wind farm connected and subsequently with the wind farm integrated. The objective is to determine the wind farm capacity at which the protection devices reach their operational limits.

Based on these results, a TEA of the SIC-SFCL is conducted. The device specifications are defined first, followed by an inventory analysis and estimation of its losses. Finally, both Capital Expenditure (CAPEX) and Operational Expenditure (OPEX) of the device are estimated.

To assess the economic feasibility of integrating the superconducting device into the power system, this solution is compared with upgrading the existing grid protection. A sensitivity analysis is also performed to evaluate the cost-effectiveness of both options under varying conditions.

Figure 3.1 illustrates the methodology, which is described in detail in the following sections.

Figure 3.1: Flowchart of the presented methodology.

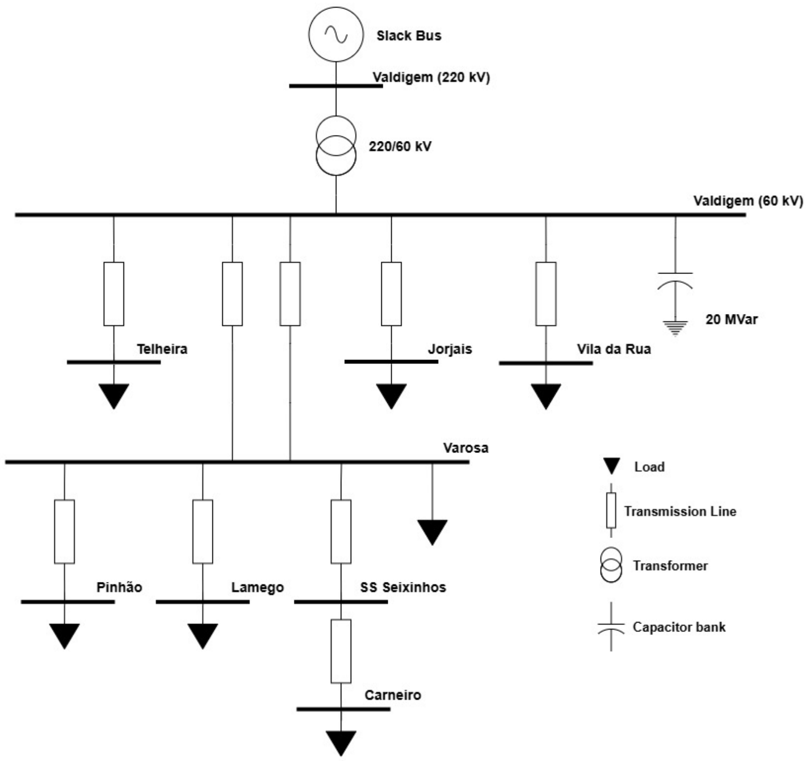

Figure 3.2: Model of grid under study.

3.2 Impact of Wind Farm Integration into the Distribution Grid

3.2.1 Modeling and Steady-State Analysis of the selected power grid

In this study, the selected power system model is based on a specific segment of the Portuguese distribution network operated by E-REDES. This segment encompasses all substations part of the Portuguese distribution network supplied by the Valdigem substation of the transmission network. The modeled network includes all downstream substations and Switching Stations (SS), representing the infrastructure responsible for the regional power distribution. The network topology and electrical parameters were based on available grid documentation and data provided by E-REDES and Rede Energia Nacional (REN) [40, 41]. Figure 3.2 shows the schematic diagram of the grid model under study.

Generator

The model under study has a single generator located at the 220 kV Valdigem busbar. This generator represents the upstream transmission grid operated by REN and supplies energy to the distribution network. To simplify the model, all power generation connected to each substation was not considered.

Table 3.1: Busbars of the grid model.

Busbars	
220 kV	**60 kV**
Valdigem	Valdigem
	Varosa
	Telheira
	Vila da Rua
	Jorjais
	Pinhão
	Lamego
	SS Seixinhos
	Carneiro

Busbars

Table 3.1 lists all busbars that comprise the grid model under study. The Valdigem transmission substation, represented by its 220 kV and 60 kV busbars, supplies the distribution substations represented by their respective 60 kV busbars. The busbars of all associated SS were also included to ensure a more realistic model.

Transformer

At the Valdigem substation, the voltage is lowered from 220 kV to 60 kV using three power transformers, whose specifications are listed in Table I.2.

To simplify the system representation, the three transformers are modeled as a single equivalent transformer formed by their parallel combination. Since TRF3 operates with a different base power than TRF1 and TRF2, its impedance and admittance must be converted to the same base power before combining them. The formulas used to convert per-unit impedance and admittance between different base powers are shown in equations 3.1 and 3.2, respectively. In these equations, Z_{new} and Y_{new} represent the impedance and admittance on the new base power S_{new}, while Z_{old} and Y_{old} refer to the original values on base S_{old}:

$$Z_{new} = Z_{old} \cdot \frac{S_{new}}{S_{old}} \tag{3.1}$$

$$Y_{new} = Y_{old} \cdot \frac{S_{old}}{S_{new}} \tag{3.2}$$

Once all values are referred to the same base, the equivalent impedance and admittance of the three transformers connected in parallel, Z_1, Z_2 and Z_3 and Y_1, Y_2 and Y_3, are calculated. Considering the rectangular form of Z and Y:

$$Z = R + jX \tag{3.3}$$

$$Y = G + jB \tag{3.4}$$

where R is the resistance, X the reactance, G the conductance, and B the susceptance.

The parallel equivalent of the impedance and the admittance, respectively, is given by:

$$\frac{1}{Z_{eq}} = \frac{1}{Z_1} + \frac{1}{Z_2} + \frac{1}{Z_3} \tag{3.5}$$

$$Y_{eq} = Y_1 + Y_2 + Y_3 \tag{3.6}$$

Last but not least, it is necessary to convert both Z_{eq} and Y_{eq} to the corresponding base power, which is the total apparent power base of the three combined transformers. This conversion was performed using equations 3.1 and 3.2.

Transmission lines

Table I.3 lists the 10 transmission lines that constitute the modeled network. Given the information provided by [40], some assumptions and adjustments related to the model were taken into account, which are described below:

- Segments with the same identification code, indicating they belong to the same transmission line, were represented as a single equivalent segment, with the total length calculated as the sum of the individual segment lengths. The cable type and cross-sectional area of the longest segment were considered representative of the entire line.
- Lines with a maximum current of zero, indicating they are non-operational, were excluded from the modeled network.
- The bare conductors for aerial power lines labeled 'AA' refer to Aluminum Conductor Steel Reinforced (ACSR).

The electrical characteristics of the ACSR conductors are represented in Table I.4.

Resistance values were obtained directly from the manufacturer's catalog [42], while the inductance and capacitance values were derived from the given inductive and capacitive reactance values, respectively, assuming a frequency of 50 Hz, based on data from [43].

Loads

Table I.5 presents the total capacity S, along with the corresponding P and Q of each substation, assuming a power factor of 0.9. For this study, it is assumed that the total capacity of each substation is equal to the S of its associated load.

Capacitor bank

The Valdigem substation includes a capacitor bank installed at the 60 kV level, with a rated capacity of 20 MVar. The respective capacitance of the capacitor bank can be estimated using equations 3.7 and 3.8:

$$Q = \frac{V^2}{X_C} \tag{3.7}$$

$$X_C = \frac{1}{2\pi f \cdot C} \tag{3.8}$$

where Q is the reactive power supplied by the capacitor bank, V is the voltage across the capacitor bank, X_c is the capacitive reactance, C is the capacitance and f.

Substituting X_c in 3.7:

$$Q = V^2 \cdot 2\pi f \cdot C \tag{3.9}$$

Solving for C:

$$C = \frac{Q}{2\pi f \cdot V^2} \tag{3.10}$$

A load flow analysis of the system is then performed, by simulation, to determine the steady-state operating conditions of the modeled power system. This analysis aims to evaluate the bus voltages magnitudes, phase angles, and active (P) and reactive (Q) power flows throughout the network. If these parameters remain within acceptable limits, it can be reasonably assumed that the system will operate stably and remain within its designated operating limits for the given configuration [44].

3.2.2 Wind farm integration

The integrated wind farm comprises Doubly-Fed Induction Generator (DFIG)–based wind turbines. The main specifications of the wind turbine and the DFIG model are provided in Table I.7.

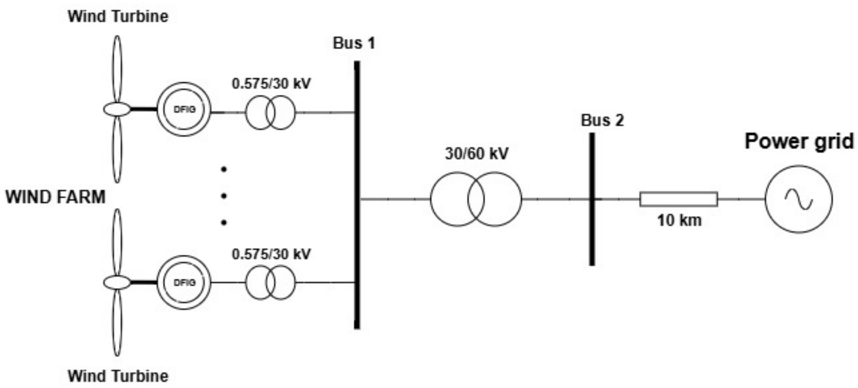

Figure 3.3: Schematic diagram of the DFIG-based wind farm integrated in the distribution network.

Each turbine is equipped with its own transformer, which steps up the voltage from 575 V to 30 kV. The power generated by the DFIG-based wind turbines is then transmitted to a grid connection substation, where another transformer increases the voltage from 30 kV to 60 kV, allowing the power to be injected into the distribution network grid. This process is illustrated in Figure 3.3.

The 60/30 kV transformer's capacity at the grid connection substation was selected based on the standard models used by E-REDES, as listed in Table I.6. The required transformer rating was defined considering the total S generated by the wind farm, with an additional 30% margin to ensure that the transformer loading does not exceed 70% of the total installed capacity under normal operating conditions. If a single transformer does not provide sufficient capacity, multiple transformers can be connected in parallel. In such cases, the equivalent impedance is calculated using the same approach described in 3.2.1.

Since the connection to the distribution network is made at the Varosa substation (60 kV), it will be assumed that the wind farm is located within a 10 km radius of Varosa.

3.2.3 Wind farm short-circuit current contribution

To assess the impact of integrating a wind farm on fault current levels and the performance of protection devices at the Varosa distribution substation, a short-circuit analysis of the wind farm's contribution was performed using MATLAB/Simulink.

A three-phase symmetrical fault with a duration of three seconds was simulated at the 60 kV busbar of the Varosa substation. This type of fault is used as the reference condition for the sizing of substation protection devices, such as circuit breakers, since it produces the highest fault currents in the system [9]. These devices must be capable of safely interrupting the maximum fault current, and their rated breaking capacity is defined based on the Root Mean Square (RMS) value of the subtransient short-circuit current (I_k'').

The study began with the simulation of a base case scenario, which represents the current power system configuration without any wind farm integration, serving as a reference for comparison. Based on the real maximum short-circuit current at the Varosa substation, presented in Table I.1, and considering the rated breaking capacity of the installed protection devices (25 kA), it was determined that an increase of 1.155 kA in the fault current would bring the system to the protection threshold. In other words, an additional 1.155 kA in the short-circuit current would cause the protection devices to reach their maximum rated breaking capacity, potentially compromising the system safety.

Following the analysis of the base case scenario, the first simulation scenario involving the integration of a wind farm was conducted. In this scenario, the theoretical wind power generation required to produce an additional short-circuit current of 1.155 kA at the Varosa substation was estimated. This estimation considered the contribution of DFIG-based wind turbines to the short-circuit current. According to existing literature, the short-circuit peak current generated by a DFIG under symmetrical fault conditions is approximately 3 p.u [45–47]. This value was adopted as a reference to determine the required generation capacity of the wind farm in the simulation scenario under consideration.

The required power generation for this scenario was estimated using the following equation:

$$P_{wf} = \sqrt{3} \cdot V_n \cdot \frac{I_{sc}}{3} \cdot \cos\phi \tag{3.11}$$

where P_{wf} represents the active power generated by the wind farm, V_n is the nominal system voltage, I_{sc} is the required short-circuit current contribution, and $\cos\phi$ is the assumed power factor.

Considering a nominal voltage of 60 kV and a power factor of 0.95, the required wind farm generation was calculated to be approximately 37.5 MW. Since the wind farm model consists of 1.5 MW DFIG-based wind turbines, twenty-five turbines were considered, corresponding to a total installed capacity of 37.5 MW.

If the simulated short-circuit current contribution from a 37.5 MW wind farm is insufficient to produce a 1.155 kA increase at the Varosa substation, a second scenario, considering a wind farm with a higher installed generation capacity, would be simulated in order to achieve the desired fault current level.

3.3 Techno-Economic Assessment of the SIC-SFCL

In order to assess the technical and economic viability of the SIC-SFCL, an Excel-based computational tool was developed. This tool is not intended for the design of the device itself; instead, it relies on input parameters derived from a previously established SIC-SFCL optimized design. These parameters are used to quantify the material requirements

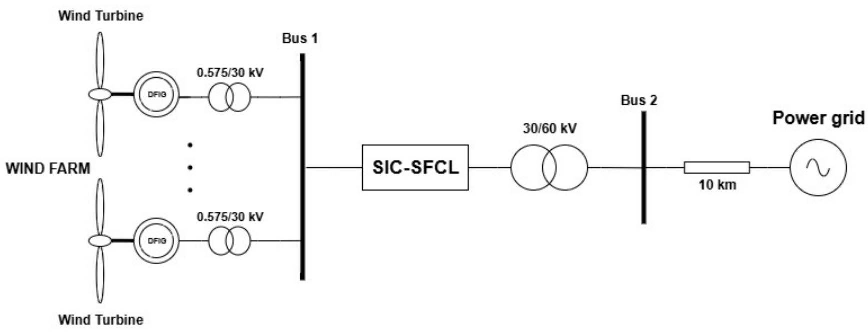

Figure 3.4: Schematic diagram of the SIC-SFCL at the grid connection substation.

for device fabrication, estimate its operational losses under steady-state conditions, and calculate the device's total cost.

3.3.1 SIC-SFCL Specifications

Following the integration of the wind farm, a SIC-SFCL is implemented. As illustrated in Figure 3.4, the device is installed at the grid connection substation on the medium-voltage side, operating at 30 kV. The rated apparent power of the SIC-SFCL is defined based on the installed generation capacity of the connected wind farm.

Two additional key specifications characterize the SIC-SFCL: the maximum limited current and the maximum expected fault current.

The maximum limited current corresponds to the peak short-circuit current at the grid connection substation, obtained through the simulation of a three-phase fault at the Varosa substation. To ensure that the limited current remains below this calculated value during a fault event, a 5% safety margin was applied, thereby establishing the maximum limited current rating of the superconducting device.

On the other hand, the maximum expected fault current was determined by simulating a three-phase fault directly at the 30 kV side of the grid connection substation and measuring the resulting I_{sc}. In this case, a 5% safety margin was considered as an upper limit in order to account for potential fault current variations.

3.3.2 Inventory analysis

The inventory of the superconducting device is conducted to quantify the manufacturing requirements of its development. To do so, the device is divided into its four main components: the iron cores, the Direct Current (DC) bias coil, the Alternating Current (AC) coils, and the cryogenic system. For each component, the material specifications and design parameters, derived from a previously optimized design of the device, were detailed.

3.3.2.1 Iron cores

To better illustrate the structural design of a SIC-SFCL, a single-phase version of the device is illustrated in Figure 3.5.

A key design aspect of the device is the cross-sectional area ratio between the DC core, AC cores, and the yokes. To ensure the AC cores operate in a deeply saturated state under normal conditions, the cross-sectional areas need to follow this hierarchy: $S_{DC} > S_{yoke} > S_{AC}$, where S_{dc}, S_{yoke} and S_{ac} represent the cross-sectional areas of the DC core, yoke, and AC core, respectively [48]. Literature suggests that the optimal ratio between the DC and AC core cross-sections typically ranges between 1.3 and 1.7, depending on the specifications of the device itself. Finite Elements Method (FEM) simulations are typically used to optimize this ratio [49–51]. Once the cross-sectional areas of the cores are determined, the total volume of the iron cores (V_{cores}) can be calculated using the following expression:

$$V_{cores} = n_{cores} \cdot (S_{dc} \cdot h_{cores} + S_{ac} \cdot h_{cores} + 2 \cdot S_{yoke} \cdot w) \tag{3.12}$$

where n_{cores} is the number of cores, h_{cores} is the height of the core, and w is the width of the inner window of the core.

The corresponding weight of the iron cores W_{cores} is then given by:

$$W_{cores} = \rho_{core} \cdot V_{cores} \tag{3.13}$$

where ρ_{core} is the density of the core material.

Since iron cores are typically manufactured from thin laminated steel sheets stacked in layers, the effective total mass of the cores m_{cores} is adjusted by the stacking factor k. The resulting effective mass is therefore:

$$m_{cores} = W_{cores} \cdot k \tag{3.14}$$

where k is the stacking factor of the iron cores material.

Typically, the iron cores of electrical machines are manufactured from grain-oriented silicon steel due to its favorable magnetic properties and low core losses. In 2024, the cost of electrical steel ranged from 2,000-3,500 €/ton, equivalent to approximately 2.21–3.86 €/kg [52].

Table 3.2 details the material and design parameters of the iron cores used in this methodology.

Table 3.2: Parameters of the iron cores.

	Parameters	Symbol	Unit
Material specifications	Density	ρ_{core}	kg/m^3
	Core Loss (1.7T/50Hz)	P_{core}	W/kg
	Stacking factor	k	-
	Cost	$c_{material}$	€/kg
Design parameters	Number of cores	n_{cores}	-
	Cross-section of DC column	S_{dc}	m^2
	Cross-section of AC column	S_{ac}	m^2
	Cross-section of yoke	S_{yoke}	m^2
	Height	h_{cores}	mm
	Inner window width	w	mm
	Volume	V_{cores}	m^3
	Weight	W_{cores}	kg
	Total mass of the cores	m_{cores}	kg

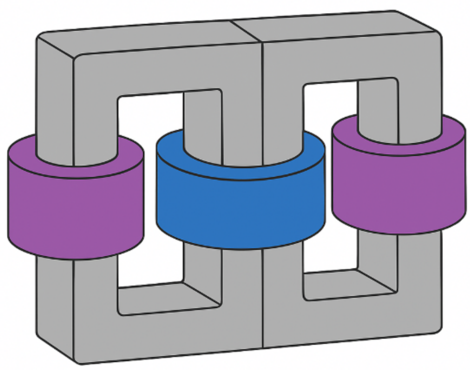

Figure 3.5: Design of a single-phase SIC-SFCL.

3.3.2.2 DC bias coil

The DC bias coil is the main component of the SIC-SFCL. Its purpose is to magnetize the iron cores into a deeply saturated state with almost no losses. This can only be achieved if the Magnetomotive Force (mmf) supplied by the DC bias coil is high enough. Achieving the same magnetizing capability with a conventional coil would require an extremely large and heavy design, with huge energy losses from Joule heating that would be unacceptably high [31].

This phase aims to estimate the total length of High Temperature Superconductor (HTS) tape required to manufacture the bias coil, using parameters based on an existing optimized design. Due to the relatively high cost of second-generation HTS materials, minimizing the amount of HTS material while ensuring adequate performance is essential for a cost-effective implementation.

The total length of HTS tape required can be approximated using the following equation:

$$l_{HTS} = n_{pancakes} \cdot f_{pancake} \cdot n_{turns} \cdot P_{turnDC} \tag{3.15}$$

where $n_{pancakes}$ is the number of stacked pancakes that make up the DC bias coil, $f_{pancake}$ is the pancake factor (equal to 1 for single pancakes and 2 for double pancakes), n_{turns} is the average number of turns per pancake, and P_{turnDC} is the perimeter of each turn.

To simplify the estimation of the turn perimeter, the average of the inner d_{inDC} and outer d_{outDC} diameter of each pancake can be considered. Therefore, the P_{turnDC} can be estimated as follows:

$$P_{turnDC} = \pi \cdot d_{pancake,avg} \tag{3.16}$$

where $d_{pancake,avg}$ is the average diameter of each pancake.

Although the cost of 2G HTS tapes remains relatively high compared to conventional materials, it has significantly decreased in recent years. In 2022, the market price of 2G HTS tapes ranged between \$100 and \$150 per $kA \cdot m$, which was around three times lower than the price 5 years before (300–500 $\$/kA \cdot m$) [53]. Assuming prices have remained relatively stable since 2022, and considering the current exchange rate, the cost in euros is estimated to be approximately between 85 and 130 $€/kA \cdot m$.

Table 3.3 shows the input parameters of the HTS coil used in this methodology.

3.3.2.3 AC coils

The AC coils of the SIC-SFCL are responsible for the current limiting process of the SIC-SFCL. Under normal operation, the AC current flowing through the AC windings-connected in series with the power grid-generates a magnetic flux that remains significantly lower than the flux produced by the DC bias coil, ensuring that the iron cores remain in a saturated state, and making the impedance of the device negligible. When the fault occurs, the fault currents produced by the fault event are high enough to drive the iron cores out of saturation alternately. This results in a substantial increase in the device's impedance, effectively limiting the fault current. Since only one core is driven out of saturation in each half-cycle while the other remains saturated, two AC coils are required, one for each core, with currents flowing in opposite directions. This arrangement allows the SIC-SFCL to

Table 3.3: Parameters of the DC bias coil.

	Parameters	Symbol	Unit
Material specifications	Critical current @77K	I_c	A
	Tape cost	c_{HTS}	€/kA·m
Design parameters	DC bias current	I_{DC}	A
	Number of pancakes	$n_{pancakes}$	-
	Turns per pancake	n_{turns}	-
	Pancake factor	$f_{pancake}$	-
	Pancake inner diameter	d_{inDC}	mm
	Pancake outer diameter	d_{outDC}	mm
	Total tape length	l_{HTS}	m

effectively limit both the positive and negative half-cycles of a single-phase fault current [54].

The material and design parameters of the AC coils are specified in Table 3.4.

The total length of conductor material $l_{conductor}$ required to manufacture each AC coil can be estimated using equation 3.17:

$$l_{conductor} = n_{turnsAC} \cdot P_{turnAC} \tag{3.17}$$

where $n_{turnsAC}$ is the number of turns per coil and P_{turnAC} is the average perimeter of a single turn.

Similar to the DC bias coil, the perimeter of each turn can be approximated by considering the average diameter of the inner (d_{inAC}) and outer (d_{outAC}) coil diameters. Thus, P_{turnAC} can be expressed as:

$$P_{turnAC} = \pi \cdot d_{AC,avg} \tag{3.18}$$

where $d_{AC,avg}$ is the average diameter of each AC coil.

Table 3.4: Parameters of the AC coils.

	Parameters	Symbol	Unit
Material specifications	Resistivity	$\rho_{conductor}$	$\Omega \cdot m$
	Cross-section	$S_{conductor}$	mm^2
	Cost	$c_{conductor}$	€/kg
Design parameters	Number of coils	n_{coils}	-
	Turns per coil	$n_{turnsAC}$	-
	Inner diameter	d_{inAC}	mm
	Outer diameter	d_{outAC}	mm
	Total length	$l_{conductor}$	m

3.3.2.4 Cryogenic system

The cryogenic system is critical for the operation of HTS devices, as it ensures that the superconducting material remains below its critical temperature. In the case of the SIC-SFCL, by maintaining extremely low operating temperatures - typically around 77 K for systems cooled with liquid nitrogen (LN_2) — the cryogenic system ensures that the HTS coil is under superconducting conditions. The design and type of cryogenic system significantly impact both the technical performance and the overall cost of the device.

For this study, the cryogenic system was divided into three main components: the cryostat, the current leads, and the cooling system.

The cryostat serves as the thermal enclosure that houses the superconducting device and ensures thermal insulation from the ambient environment. It typically features a vacuum-insulated chamber with multilayer insulation to minimize heat input. Within the cryostat, the DC bias HTS coil is immersed in sub-cooled LN_2, ensuring it remains in the superconducting state [39, 55].

Table 3.5 details the material and design specifications of the cryostat.

The current leads provide a physical and electrical connection between the external power source at room temperature and the superconducting device inside the cryostat, which operates at very low temperatures [56]. Table 3.6 details the specifications of the current leads.

The cooling system is responsible for maintaining the cryogenic temperature in the system. There are two main types of cooling systems: open-cycle and closed-cycle. The fundamental difference between both types lies in how the evaporated cryogen is managed and how the system maintains its operating temperature. In an open-cycle cooling system, the evaporated LN_2 is released directly into the atmosphere, requiring regular refilling

Table 3.5: Parameters of the cryostat.

	Parameters	Symbol	Unit
Material specifications	Apparent thermal conductivity	λ	$W/m \cdot K$
Design specifications	Height	h_{cryo}	mm
	Inner diameter	$d_{in,cryo}$	mm
	Outer diameter	$d_{out,cryo}$	mm
	Thickness of the vacuum insulation layer	δ	mm
	Equivalent heat transfer area	A	m^2

Table 3.6: Parameters of the current leads.

	Parameters	Symbol	Unit
Specifications	Heat input	Q_{cl}	W/kA
	Number of current leads	n_{cl}	-

of liquid LN_2. These systems are generally simple, cost-effective, and highly reliable. In contrast, a closed cryogenic system captures and re-liquefies the evaporating LN_2 using a cryocooler, eliminating the need for frequent LN_2 refills. Although closed-cycle cooling systems are more complex and involve a higher initial cost, the advantage of not requiring regular LN_2 refills represents a major benefit, particularly for long-term, unattended operation in power grid applications [55, 57].

The cryocooler, presented only in closed systems, is responsible for continuously maintaining the required low temperatures by extracting heat from the cryostat volume and re-condensing the evaporated nitrogen. Several types of cryocoolers are commonly used, each based on different thermodynamic principles: Gifford-McMahon, Pulse Tube, Stirling, and Turbo-Brayton [58]. The cost the cooler operating at 77 K can be estimated as [59]:

$$c_{cryocooler}(k€) = 1.54 \cdot P_{th}^{0.57} \tag{3.19}$$

where $c_{cryocooler}$ is the cost of the cryocooler in thousands of euros and P_{th} is the cooling capacity of the device.

This expression was adapted from USD to EUR, with the currency conversion updated to present values.

Table 3.7 shows the main technical parameters of a cooler.

Table 3.7: Parameters of the cryocooler.

	Parameters	Symbol	Unit
Technical specifications	Cooling capacity	P_{th}	W
	Efficiency	η	%

Although this analysis focuses on the cryostat, current leads and the cooling system as the main components of the open cryogenic system, it is important to acknowledge that a complete setup typically includes other supporting elements such as an LN_2 storage tank, valves, vacuum pumps, insulation pipes, and sensors.

Estimating the cost of a full cryogenic system is not straightforward. Since these systems are often custom-designed for specific applications, defining a representative generic cost is particularly challenging. For this reason, and to simplify the present analysis, cost estimates for the cryogenic system were either obtained directly from qualified suppliers, taking into account the specifications of each component, or considered by assumption. In the case of closed-cycle systems, the cost of the cryocooler was also included into the total system cost.

3.3.3 Loss Estimation

Estimating the losses in the SIC-SFCL is crucial to accurately assess the device's performance and efficiency during steady-state conditions. Since the HTS coil operates with a constant DC current source, there are no losses in the HTS coil. However, the device is not lossless. The losses in the SIC-SFCL during normal conditions are:

Core Losses in the Iron Core

Core losses refer to the energy dissipated in the magnetic core material when subjected to alternating magnetic fields. These losses are primarily composed of two components:

$$P_{core} = P_{hyst} + P_{eddy} \tag{3.20}$$

where P_{hyst} represent the hysteresis losses and P_{eddy} the eddy current losses.

Hysteresis losses (P_{hyst}) are caused by the continuous magnetization and demagnetization of the core material as the AC magnetic field reverses direction, while the eddy current losses (P_{eddy}) are caused by circulating currents induced within the core material itself by the changing magnetic field. As both types of losses are intrinsically linked to the magnetic and electrical properties of the core material, the total core losses are typically estimated using specific loss data provided in the material's datasheet.

Joule Losses in the AC Coils

These losses occur due to the resistance of the conductor when alternating current flows through it. Hence, the joule losses in the AC coils can be estimated based on equation 3.21 :

$$P_{jAC} = I_n^2 \cdot R \tag{3.21}$$

In this expression, I_n represents the nominal AC current flowing through the coils, and R is the total resistance of the conductor used in all the AC coils.

The resistance of the AC coils is determined using equation 3.22:

$$R_{ACcoils} = \rho_{conductor} \cdot \frac{l_{conductor}}{S_{conductor}} \tag{3.22}$$

where $\rho_{conductor}$ is the electrical resistivity of the conductor, $l_{conductor}$ represents the total length of the conductor used in the AC coils, and $S_{conductor}$ is the cross-sectional area of the conductor.

Heat input

The total heat input to the cryogenic system of the SIC-SFCL consists primarily of two components: the heat input from the cryostat and the current leads.

The heat input through the cryostat is estimated using Equation 3.23:

$$Q_{cryostat} = \frac{\lambda \cdot A \cdot \Delta T}{\delta} \tag{3.23}$$

where λ represents the apparent thermal conductivity of the cryostat, $A = \sqrt{A_{\text{in}} \cdot A_{\text{out}}}$ is the equivalent heat transfer area—calculated as the geometric mean of the inner (A_{in}) and outer (A_{out}) surface areas of the cryostat—ΔT is the temperature difference across the insulation layers, and δ is the total thickness of the vacuum insulation [39].

The heat input from the current leads (Q_{cl}) is estimated separately, as it results from the heat conducted along the metallic leads that connect the external power source to the superconducting coil. Two main contributions are involved: Joule heating and thermal conduction. Optimizing current leads essentially requires choosing the conductor dimensions so that Joule heating and thermal conduction are balanced for a given level of electrical current. In this way, the overall heat input can be minimized by selecting an appropriate ratio between the lead's length and cross-sectional area [56, 60].

The minimum heat input from conduction-cooled conventional current leads can be determined as shown in Equation 3.24 [56, 61]:

$$Q_{cl} = I\sqrt{L_0 \cdot (T_H^2 - T_C^2)} \tag{3.24}$$

In this equation, I represents the rated transport current (in this case, the DC bias current I_{DC}), while L_0 is the Lorenz number (a constant). The terms T_H and T_C represent the temperatures of both the warm and cold end of the current lead, respectively.

For conventional conduction-cooled current leads cooled at the LN_2 temperature (77K) the minimum heat input is 45 WkA^{-1}.

The heat input causes the evaporation of LN_2. In an open cryogenic system, losses are quantified by the total amount of LN_2 required to refill the system, while in a closed system, losses are estimated based on the electrical power consumption of the cryocooler (P_{el}). Theoretically, the electrical power consumption of the cryocooler is calculated considering the efficiency of the cryocooler (η), as demonstrated in Figure 3.25 :

$$P_{el} = \frac{P_{th}}{\eta} \tag{3.25}$$

3.3.4 CAPEX and OPEX estimation

The next step is to evaluate the capital and operational costs associated with the implementation of the SIC-SFCL. The CAPEX includes all material and construction costs, while the OPEX accounts for recurring expenses such as energy consumption and maintenance.

3.3.5 Economic analysis: Upgrading grid protection vs SIC-SFCL integration

3.3.5.1 Investment Requirements for Grid Protection Upgrades

The cost analysis of the protection of the grid in the distribution network was based on the "Distribution Grid Development and Investment Plan – 2024" (known as PDIRD-E), provided by E-REDES [62]. This document outlines the five-year investment strategy for the Portuguese distribution grid, with the aim of ensuring its safety, reliability, and overall efficiency.

The CAPEX of each future investment is divided into two categories: primary costs and total costs. Primary costs comprise material and labor expenses, whereas total costs include the primary costs plus direct, transversal, and financial charges.

For the purpose of this study, only the primary costs were considered.

The referenced document highlights a future investment in the replacement of protection equipment at a distribution network substation. This project involves the replacement of five circuit breakers, ten disconnectors, and fifteen instrument transformers (current transformers) in a substation with a rated breaking capacity of 25 kA. The primary costs for this investment are estimated at approximately 2,000 k€.

Considering the standard configuration of a bay adopted by E-REDES—comprising one high-voltage circuit breaker, two disconnectors, and three instrument transformers—it it is assumed that the primary cost of replacing a single bay in a 25 kA-rated substation is approximately 400 k€.

3.3.5.2 Evaluation of Economic Performance Indicator

In this section, the economic performance indicator was calculated to evaluate the most cost-effective and reliable solution. For this purpose, the Life-cycle cost (LCC) indicator was considered.

The LCC of a system represents the total present value of all expenses incurred over a time horizon [63]. It is defined as:

$$LCC \triangleq \sum_{t=0}^{H_t} \frac{C_t}{(1+r)^t} \tag{3.26}$$

where C_t are the costs in year t, r is the discount rate, and H_t is the time horizon. Since all cost terms are non-negative, the resulting LCC is inherently positive.

The costs associated with the device can be categorized into CAPEX and OPEX. CAPEX is incurred entirely at the beginning of the project (initial investment), while OPEX represents recurring annual costs, starting in the first year $t = 1$, remaining constant over time. It is assumed that the time horizon is equal to the system lifetime. Taking this into account, equation 3.26 can be rewritten as:

$$LCC = CAPEX_0 + \sum_{t=1}^{T_l} \frac{OPEX_t}{(1+r)^t} \tag{3.27}$$

where T_l is the systems lifetime, $CAPEX_0$ is the capital expenses in year zero and $OPEX_t$ is the operating expenses in year t.

To analyze the results, a sensitivity analysis was performed to compare the cost-effectiveness of both solutions under varying conditions.

4

Case Study: Results analysis

4.1 Analysis of the Impact of Wind Farm Integration into the Distribution Grid

4.1.1 Modeling and Steady-State Analysis of the selected power grid

The power grid model used in this study, representing the distribution network supplied by the Valdigem transmission substation, was implemented in MATLAB/Simulink, as shown in Figure 4.1.

The equivalent 220 kV/60 kV power transformer and the 20 MVar capacitor bank connected to the 60 kV busbar at the Valdigem substation were both dimensioned following their own methodologies presented in Section 3.2.1. The transformer's electrical characteristics are summarized in Table 4.1, while the capacitor bank sizing resulted in a total capacitance of 17.68 μF.

For the load flow analysis, base voltages were defined as 220 kV for the 220 kV bus and 60 kV for the 60 kV buses, and all load buses were modeled as PQ buses. To ensure that the voltage at all load buses remained above the operational limit between 0.97 p.u and 1.05 p.u, the voltage of the slack bus (Valdigem 220 kV) was set at 1.08 p.u.

The results of the steady-state analysis are presented in Table 4.2. All bus voltages remained between 0.97 p.u and 1.05 p.u, representing a realistic range and indicating an adequate voltage regulation throughout the network. The interconnection buses — Valdigem (60 kV) and Seixinhos — are not associated with local generation or consumption, and therefore

Table 4.1: Parameters of the Valdigem's power transformer.

Transformers	**Voltages prim/sec (kV)**	**Nominal Power (MVA)**	**R (p.u)**	**X (p.u)**	**G (p.u)**	**B (p.u)**
TRF Valdigem	220/60	466	0.0032	0.1590	0.0004	0.0017

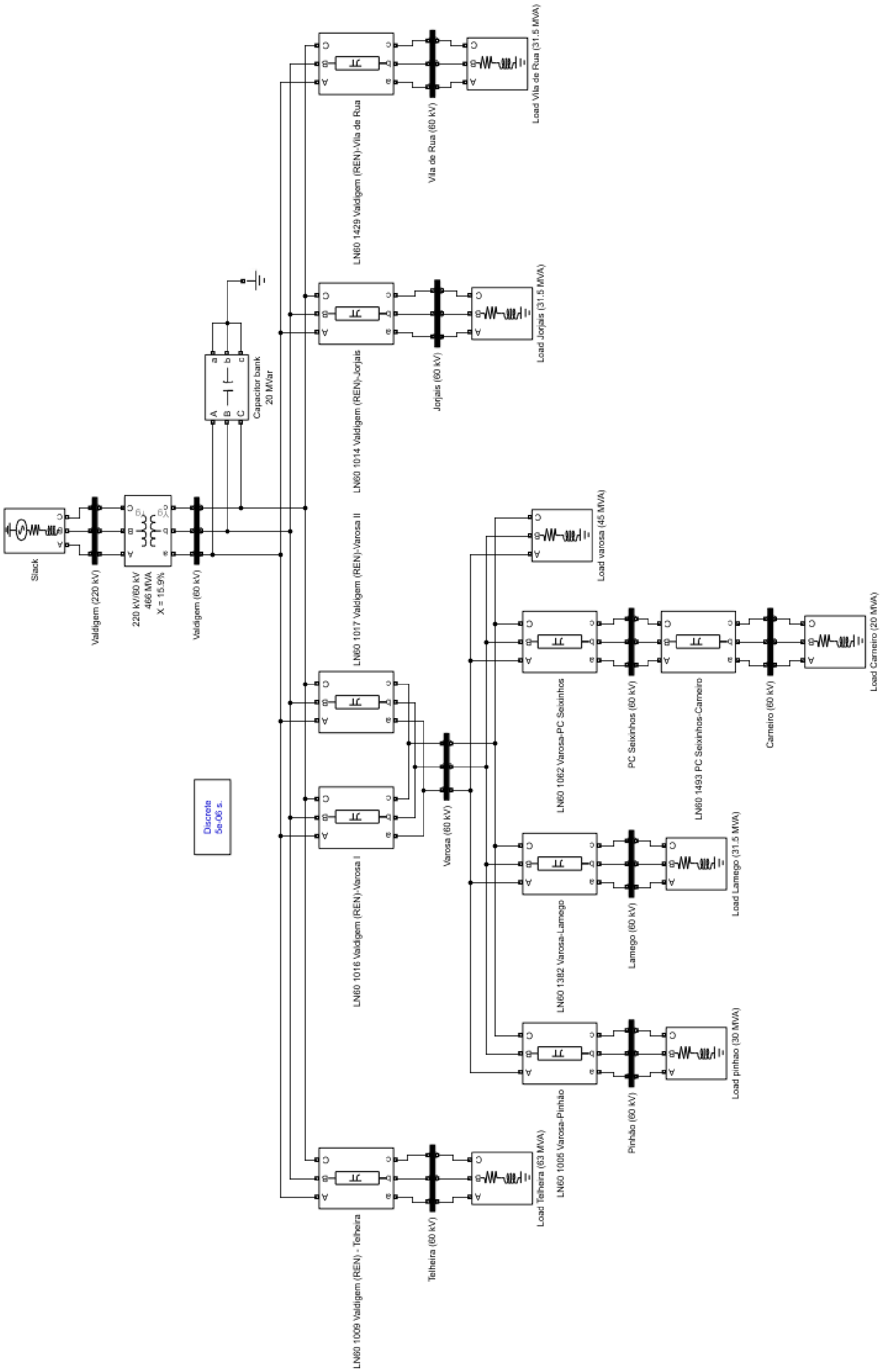

Figure 4.1: Simulink model of the grid under study.

Table 4.2: Results of the load flow analysis.

Bus	V (p.u)	θ (Deg)	P (MW)	Q (MVar)
Valdigem (220 kV)	1.080	0.000	235.326	143.726
Valdigem (60 kV)	1.047	-8.464	0.000	0.000
Telheira	0.973	-11.694	56.700	27.461
Jorjais	0.993	-10.839	28.350	13.731
Vila de Rua	0.986	-11.177	28.350	13.731
Varosa	1.041	-8.709	40.500	19.615
Lamego	1.026	-9.228	28.350	13.731
Pinhão	0.982	-10.776	27.000	13.077
Seixinhos	1.014	-9.632	0.000	0.000
Carneiro	1.000	-10.144	18.000	8.718

exhibit zero active and reactive power injection in the load flow results.

The voltage phase angle results indicate that power flows from the slack bus to the loads, as the angles at all load buses are negative. This confirms that the slack bus is actively injecting power into the system.

4.1.2 Wind Farm integration

A Doubly-Fed Induction Generator (DFIG)-based wind farm was integrated into the grid and connected to the Varosa substation. Figure 4.2 shows the Simulink model of the wind farm. The wind speed is maintained constant at 15 m/s and the reactive power Q produced by the wind farm was regulated at 0 MVar. The wind farm's P and Q output is illustrated in Figure 4.3. It shows that each wind turbine reaches its maximum P output, 0.98 p.u, at t=3s, and the Q is nearly zero.

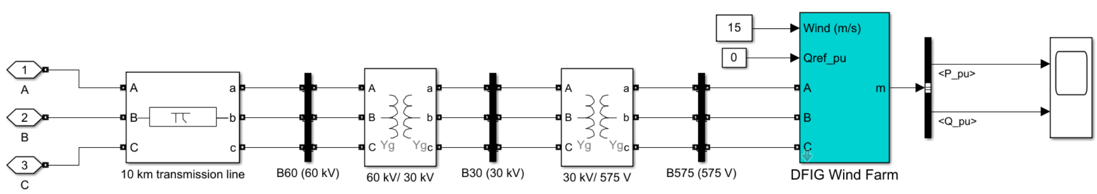

Figure 4.2: Simulink model of the wind farm.

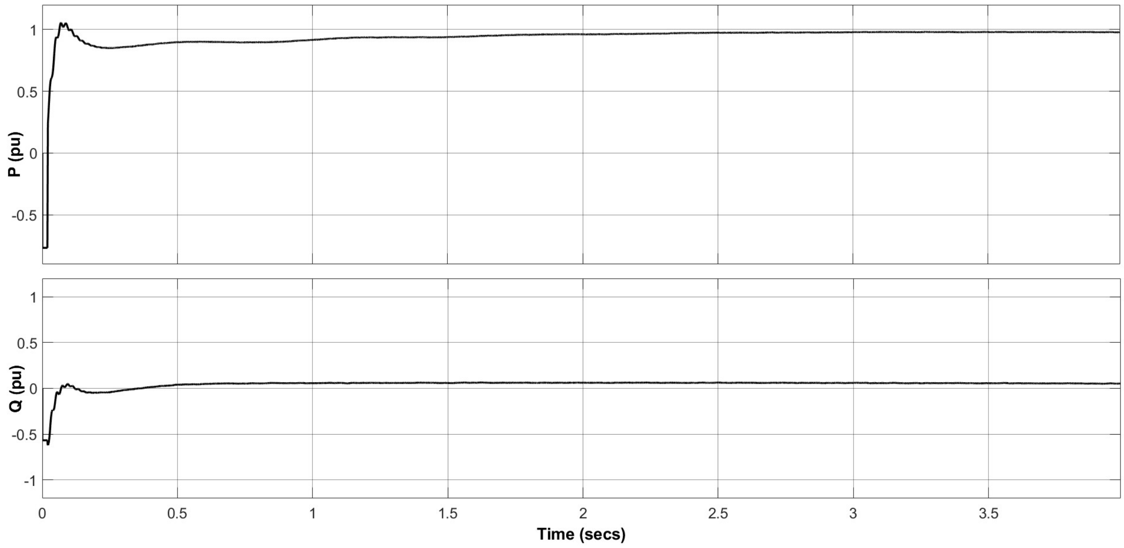

Figure 4.3: Active and reactive power generated by the wind farm.

4.1.3 Wind farm short-circuit current contribution

The fault analysis of the network supplied by the Valdigem substation was performed using a transient simulation. The upstream power grid was represented by a three-phase voltage source with a rated short-circuit capacity of 8,116 MVA (corresponding to Valdigem's maximum S_{sc}) and an X/R ratio of 10.

Consistent with the load flow analysis, and given the radial configuration of the studied network—where no voltage support from other parts of the grid is available—the generator voltage was set to 238 kV, representing approximately an 8% increase over the nominal grid voltage of 220 kV. This adjustment was introduced to compensate for voltage drops along the transmission lines and to ensure that the voltage at all busbars remains within acceptable limits.

In the base case scenario, where no wind farm is integrated into the power system, a fault analysis was performed. A symmetrical three-phase fault with a duration of three seconds was applied at the Varosa busbar at t=4s to determine I_{sc} at the substation. Figure 4.4 illustrates the simulated subtrasient fault current at the Varosa substation during the fault event, which reached a peak value of 16.82 kA.

Although the simulated model represents an actual section of the Portuguese distribution grid, not all network contributions were included. Therefore, it is expected that the resulting I_{sc} does not exactly match the value shown in I.1. However, for the purpose of this study, the resulting 16.82 kA was considered as a representation of the actual I_{sc} at the Varosa substation.

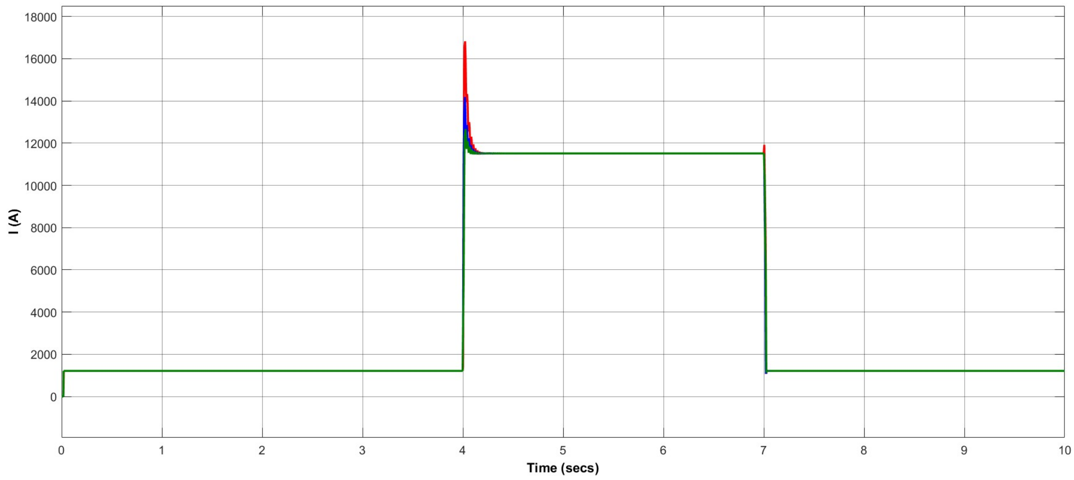

Figure 4.4: Current at the Varosa substation under a fault event without wind farm integration.

4.1.3.1 Scenario 1: 37.5 MW wind farm

A wind farm comprising twenty-five 1.5 MW DFIG-based wind turbines—totaling 37.5 MW of installed capacity—was integrated into the distribution network through the Varosa substation. At the grid connection substation, two power transformers rated at 20 MVA and 31.5 MVA were installed in parallel, providing a combined capacity of 51.5 MVA. The equivalent impedance of the two transformers in parallel, calculated as described in Section 3.2.1, was determined to be 11.39%.

The total active power injected into the distribution grid by the wind farm is presented in Figure 4.5.

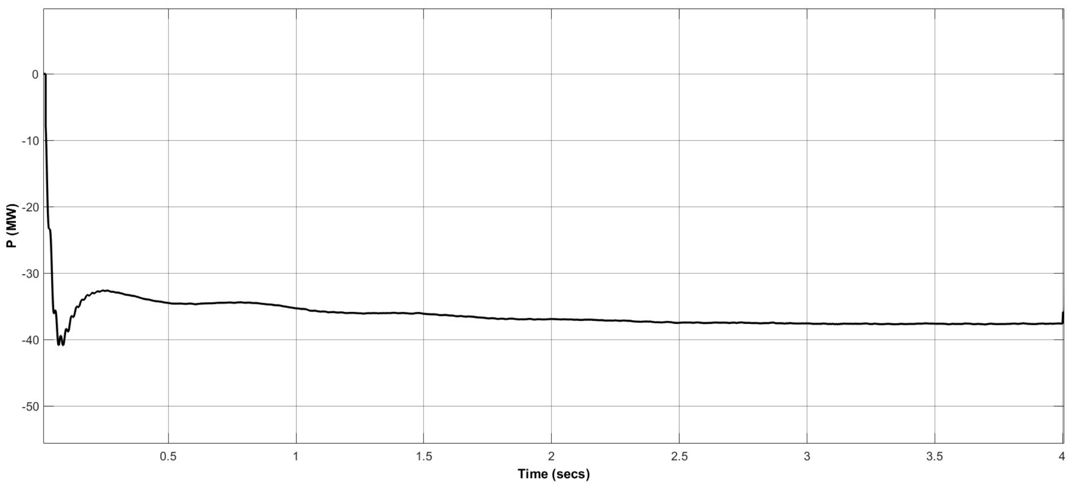

Figure 4.5: Active power generated by the 37.5 MW wind farm.

A three-phase symmetric fault lasting three seconds was simulated at the Varosa substation at t=4s.

Figure 4.6 shows the fault current generated from the wind farm. The subtransient Root Mean Square (RMS) component of the short-circuit current (I_k'') peaks at 960.1 A. Given that the pre-fault (steady-state) current is around 368 A, this corresponds to a fault current contribution of approximately 2.61 p.u (for a base apparent power of 100 MVA).

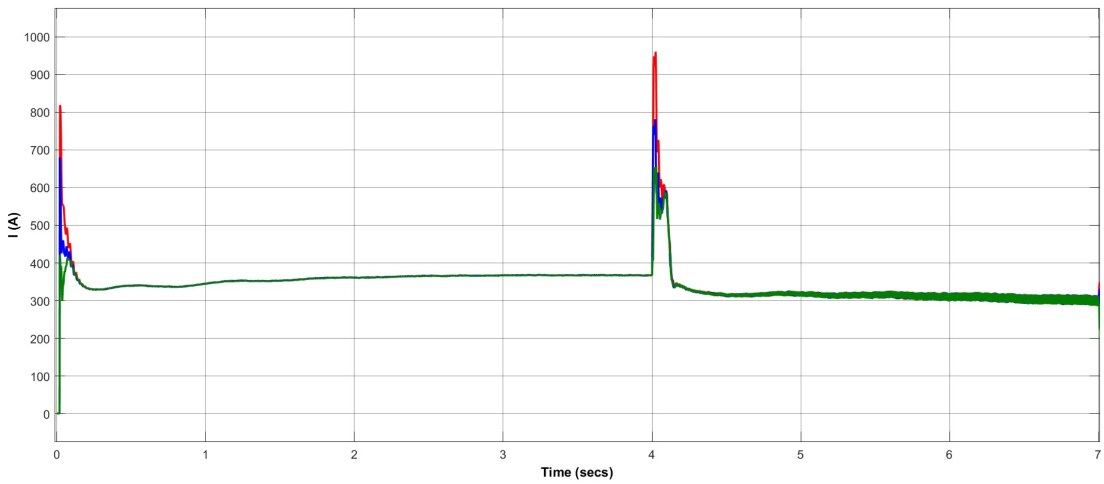

Figure 4.6: Current contribution from the 37.5 MW wind farm at the Varosa substation during the fault.

Following the integration of the 37.5 MW wind farm, the total subtrasient fault current at the Varosa substation increased to 17.62 kA. The wind farm's contribution to this value is 800 A, which represents 83.32% of the total subtrasient fault current it generates, since the rest flows to other parts of the network. Figure 4.7 shows the resulting fault current at the Varosa substation with the integration of the 37.5 MW wind farm.

Since an increase of 1.155 kA in the short-circuit current at the Varosa substation would cause the installed protection devices to exceed their rated breaking capacity, the integration of a 37.5 MW wind farm is insufficient. Therefore, a second wind farm with a higher installed capacity was analyzed.

4.1.3.2 Scenario 2: 63 MW wind farm

The number of DFIG-based wind turbines has now increased to forty-two, resulting in a total installed capacity of 63 MW.

To accommodate this generation level, the transformer capacity at the grid connection substation has been increased. The required capacity is now 91.5 MVA. This is achieved through the parallel of three transformers rated at 40 MVA, 31.5 MVA, and 20 MVA, respectively. As detailed in Section 3.2.1, the equivalent impedance of these three transformers in parallel was calculated to be 12.73%.

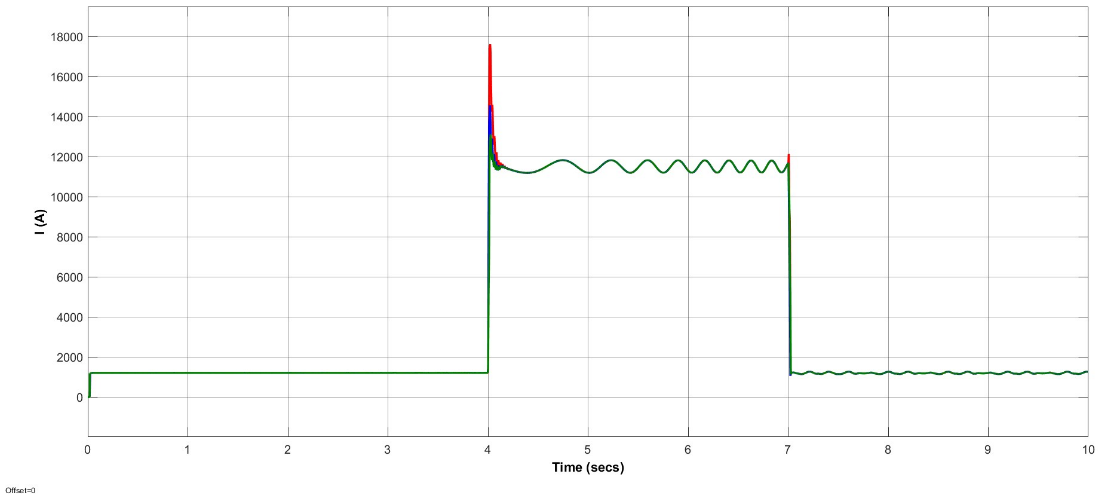

Figure 4.7: Current at the Varosa substation during a fault event with the integration of a 37.5 MW wind farm.

Figure 4.8 illustrates the total active power injected into the grid from the wind farm at the Varosa substation.

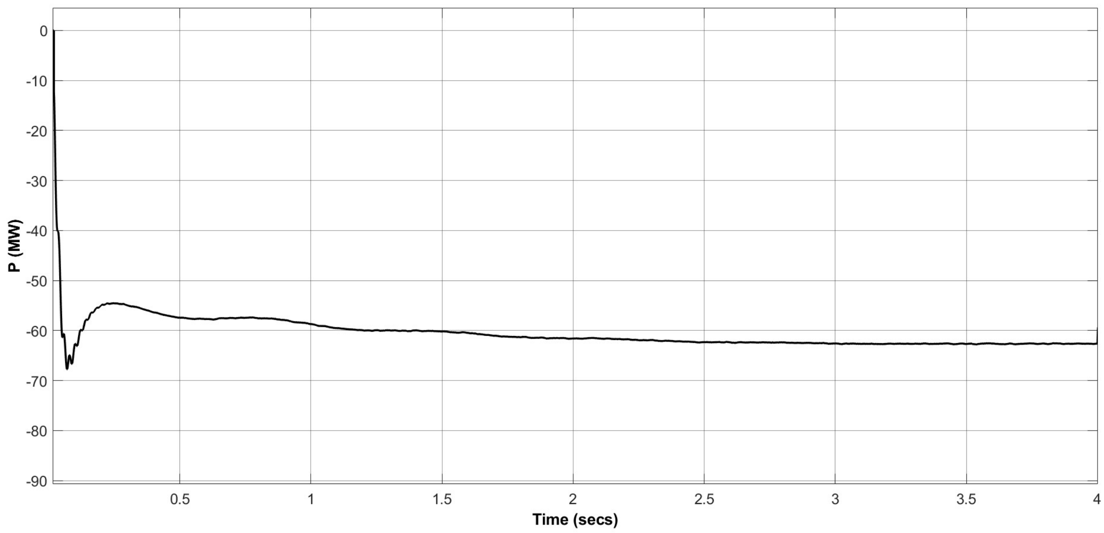

Figure 4.8: Active power generated by the 63 MW wind farm.

A three-phase symmetrical fault lasting three seconds was simulated at the Varosa substation at t=4s.

Figure 4.9 shows the fault current generated from the wind farm. The subtransient RMS component of the short-circuit current (I''_k) peaks at 1.505 kA. Given that pre-fault (steady-state) current is around 620 A, this corresponds to a fault current contribution of approximately 2.43 p.u (for a base apparent power of 100 MVA).

At the Varosa substation, the resulting subtrasient fault current increased to 18.04 kA due to the integration of the 63 MW wind farm. This means the integration of the 63 MW wind

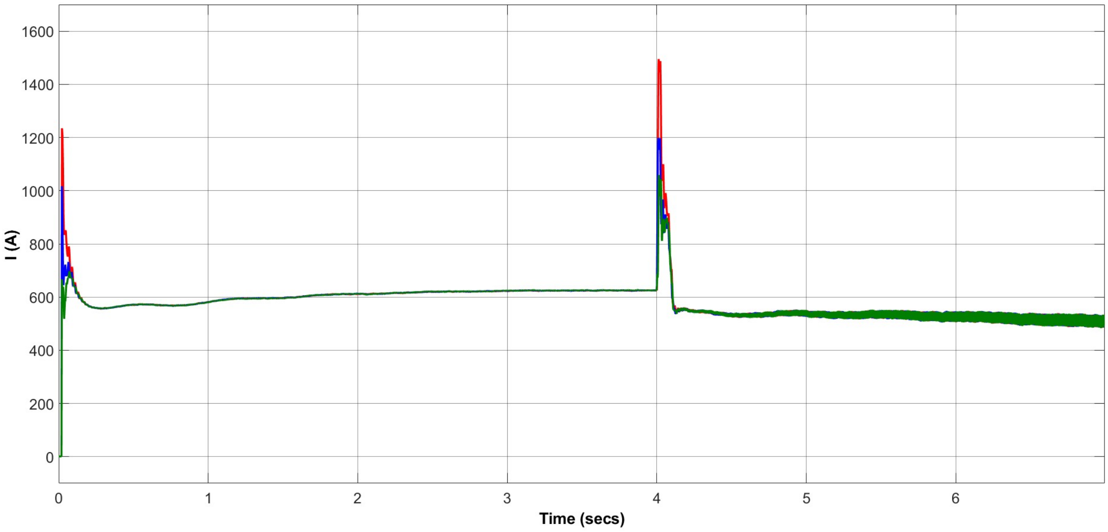

Figure 4.9: Current contribution from the 63 MW wind farm at the Varosa substation during the fault.

farm contributed with a total of 1.22 kA to the total subtrasient fault current at the Varosa substation. This value represents only 81.06% of the fault current generated by the wind farm that contributes to the short-circuit current at the Varosa substation, meaning the rest flows to other parts of the network. Figure 4.10 shows the fault current at the Varosa substation with the integration of the 63 MW wind farm.

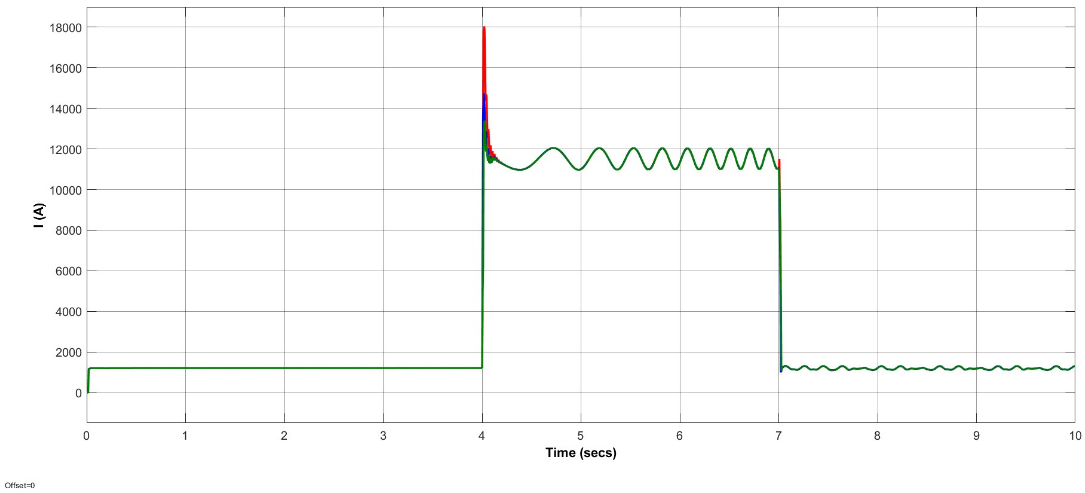

Figure 4.10: Current at the Varosa substation during the fault.

Hence, a 63 MW wind farm would cause the installed protection devices of the Varosa substation to exceed their rated breaking capacities.

4.2 Techno-Economic Assessment of a SIC-SFCL

4.2.1 SIC-SFCL Specifications

To avoid the need to upgrade the protection devices at the Varosa substation to the next standard level (breaking capacity of 31.5 kA), a Saturated Iron Cores Superconducting Fault Current Limiter (SIC-SFCL) can be integrated into the grid.

The main specifications of the SIC-SFCL are:

- Rated voltage - Since the device is intended to be installed at the 30 kV level in the grid connection substation, the rated voltage was set to 36 kV, considering a 20% design margin.
- Rated apparent power - Based on the results from the previous section and assuming a power factor of 0.95 for the DFIG-based wind farm, the rated apparent power of the SIC-SFCL was set to 70 MVA.
- Maximum limited current.
- Maximum expected fault current.

To determine the maximum limited current of the SIC-SFCL, the fault current at the 30 kV busbar of the grid connection substation was measured during a fault event located at Varosa's 60 kV busbar. A three-phase symmetrical fault with a duration of three seconds was simulated (at t=4s), and the resulting RMS short circuit current (I_{sc}) at the 30 kV busbar was 3.01 kA, as shown in Figure 4.11. To ensure this current is never reached, the maximum limited current of the SIC-SFCL was set to 2.86 kA (RMS), introducing a 5% safety margin.

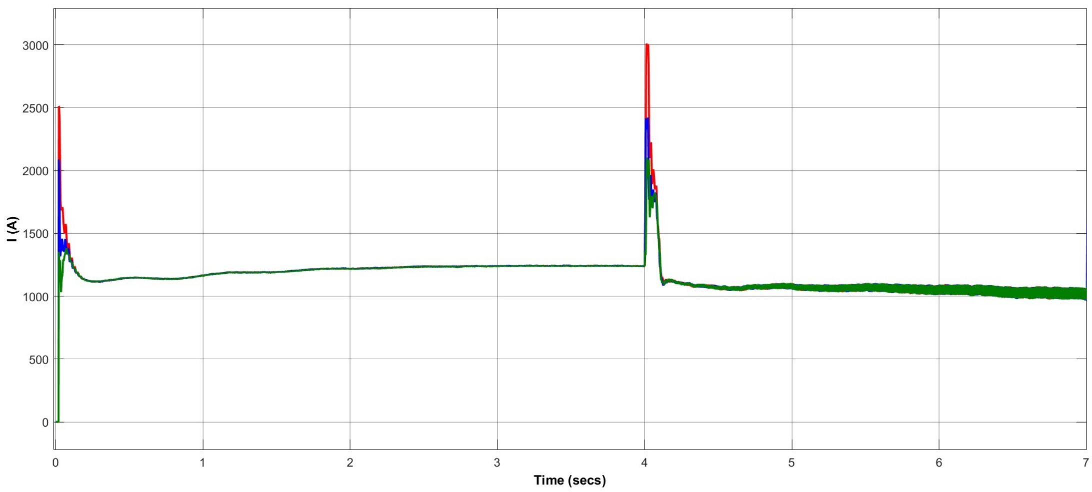

Figure 4.11: Current at the 30 kV busbar under a fault event at the Varosa busbar.

Table 4.3: General specifications of the SIC-SFCL.

Specifications	**Value**	**Unit**
Rated voltage	36	kV
Apparent power	70	MVA
Max. limited current	2.86	kA
Max. expected fault current	6.67	kA

To estimate the maximum expected fault current, the same three-phase symmetrical fault with a duration of three seconds (at t=4s) was simulated directly at the 30 kV side of the grid connection substation, in order to get maximum I_{sc} possible. The resulting RMS fault current was 6.35 kA, as shown in Figure 4.12. As mentioned in Section 3.3.1, a 5% margin was applied to account for potential fault current variations. Thus, the maximum expected fault current was set to 6.67 kA (RMS).

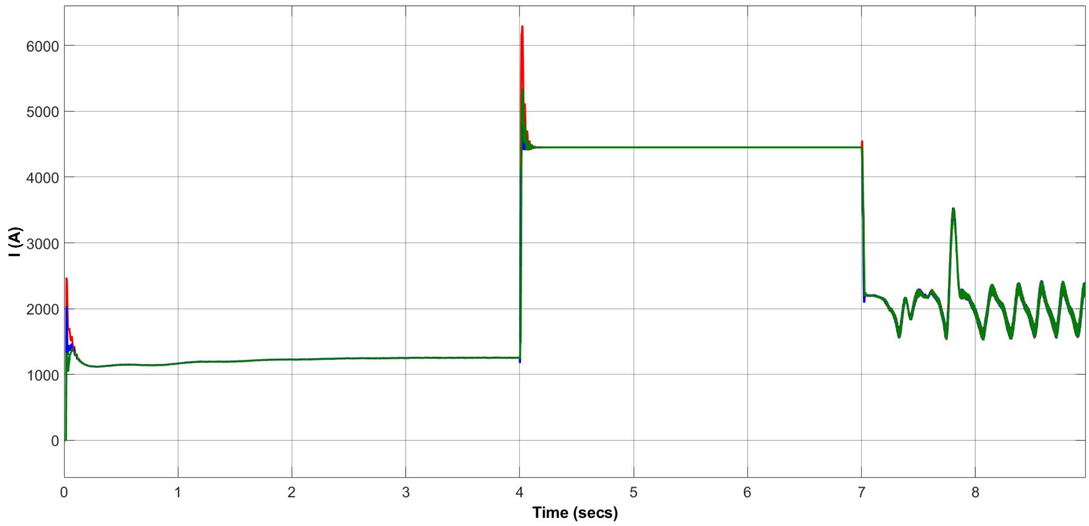

Figure 4.12: Current at the 30 kV busbar under a fault at the grid connection substation.

This means the SIC-SFCL must be capable of limiting approximately 57% of the RMS fault current.

Table 4.3 summarizes the specifications of the SIC-SFCL.

For the purposes of this study, the SIC-SFCL developed by Innopower (mentioned in Section 2.2.3) was adopted as a reference model, as its steady-state grid specifications closely align with the requirements of the case under study.

4.2.2 Inventory analysis

In this section, the inventory of the SIC-SFCL, based on the 35 kV/90 MVA model developed by Innopower, was compiled to quantify the materials required for the manufacturing of each main component of the device and estimate its associated costs.

The conditions for this analysis are described as follows:

- All technical specifications of the design under study were obtained from published sources on the device's development. When data were missing or insufficiently specified, values were inferred from the available design information and, when necessary, estimated using the methodology described in Section 3.3.

- All information on the cost of the materials and components of the device was estimated from the information already given in Section 3.3, or, when unavailable, estimated from assumptions.

4.2.2.1 Iron cores

The three-phase SIC-SFCL developed by Innopower is composed of six iron-core frames arranged in a hexagonal configuration. The Direct Current (DC) limbs of these frames are displayed adjacently, forming the central column located at the center of the hexagon. To minimize the overall diameter of this central column, the six DC limbs are configured in a fan-shaped arrangement with an injection angle of 60º. Figure 4.13 illustrates the top view of the SIC-SFCL [31].

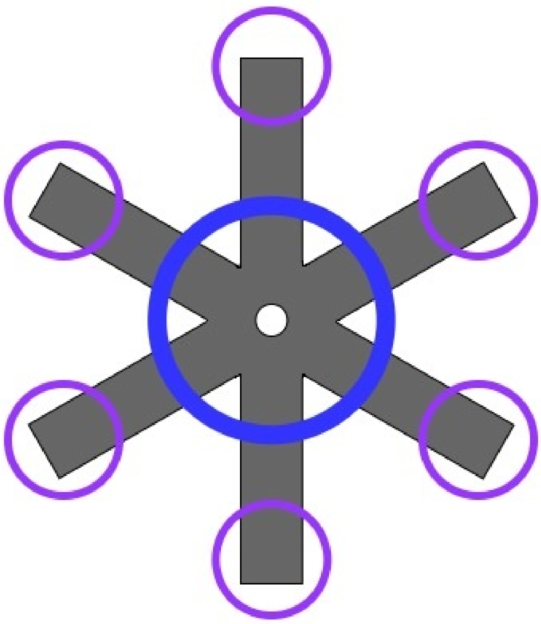

Figure 4.13: Top view of the SIC-SFCL.

Table 4.4: Parameters of the iron cores.

	Parameters	Symbol	Value	Unit
Material specifications	Density	ρ_{core}	7,650	kg/m^3
	Core Loss (1.7T/50Hz)	P_{core}	1.05	W/kg
	Stacking factor	k	0.95	-
	Cost	$c_{material}$	3.0	€/kg
Design parameters	Number of cores	n_{cores}	6	-
	Cross-section of DC limb	S_{dc}	0.11	m^2
	Cross-section of AC limb	S_{ac}	0.07	m^2
	Cross-section of yoke	S_{yoke}	0.09	m^2
	Height	h_{cores}	3,200	mm
	Inner window width	w	700	mm
	Volume	V_{cores}	4.22	m^3
	Weight	W_{cores}	32,283	kg
	Total mass of the cores	m_{cores}	30,669	kg

Due to the lack of detailed data regarding the cross-sectional areas of the limbs, the diameter of the central column was assumed to correspond to the inner diameter of the cryostat (1,160 mm). Additionally, the cross-sectional area of the central column was considered to be approximately 60% of the total cross-sectional area of the cryostat, resulting in an estimated S_{dc} of 0.11 m^2.

The cross-sectional area of the AC limb (S_{ac}) was derived from the ratio between S_{dc} and S_{ac}, as described in Section 3.3.2.1, assuming that S_{dc} is 1.6 times larger than S_{ac}. The cross-sectional area of the yoke (S_{yoke}) was assumed to lie between the values of S_{dc} and S_{ac}.

Regarding the geometry of the iron cores, the height of the iron cores h_{cores} was considered as the total height of the device excluding the external shell (3,200 mm). The width of the inner window (w) was assumed to be 700 mm, considering the total diameter of the device is 3,000 mm (excluding the external shell), and the dimensions of the cryostat.

As the core material is not specified in the available literature, it was assumed to be B30P105 grain-oriented silicon steel. Based on these assumptions, the effective total mass of the iron cores was estimated at 30,669 kg.

Table 4.4 shows the parameters of the iron cores used for this study.

Table 4.5: Parameters of the DC bias coil.

	Parameters	Symbol	Value	Unit
Material specifications	Critical current @77K	I_c	150	A
	Tape cost	c_{HTS}	100	€/kA·m
Design parameters	DC bias current	I_{DC}	300	A
	Number of pancakes	$n_{pancakes}$	44	-
	Turns per pancake	n_{turns}	54	-
	Pancake factor	$f_{pancake}$	2	-
	Pancake inner diameter	d_{inDC}	1,280	mm
	Pancake outer diameter	d_{outDC}	1,340	mm
	Total tape length	l_{HTS}	17,600	m

4.2.2.2 DC bias coil

The DC bias coil developed by Innopower is composed of 44 double-pancake coils, grouped into five sets connected in parallel. Each set was designed to carry a current of 60 A, resulting in a total DC bias current of 300 A. The coil was designed to generate a total Magnetomotive Force (mmf) of 14,1000 ampere-turns, ensuring sufficient magnetic biasing for the operation of the SIC-SFCL. Since the total effective number of turns is 470, and the turns of each ring were not necessarily the same (rings with tape connected in series or in parallel), it was assumed that the average number of turns per set is 470, leading to a total of 2,350 turns across the entire DC bias coil (around 54 turns per pancake).

The inner (d_{inDC}) and outer (d_{outDC}) diameters of the pancakes were assumed to match the inner and outer diameters of the complete DC coil.

The High Temperature Superconductor (HTS) tape used by Innopower is a 1G Bi-2223 tape, as the device was developed in the early 2000s. However, as of 2025, 2G HTS tapes are widely available and offer improved performance and cost-efficiency. Therefore, for this study, a 2G HTS tape based on GdBaCuO was considered.

Based the methodology proposed in 3.3.2.2, and the parameters derived from the Innopower prototype, the estimated length of HTS tape (l_{HTS}) is 19,557 m. This is approximately 11% less compared to the actual length of HTS tape used by Innopower, which was 17,600 m. For the purposes of this study, the actual tape length employed in the Innopower prototype was adopted.

Table 4.5 shows the parameters of the DC bias coil used for this study.

Table 4.6: Parameters of the AC coils.

	Parameters	Symbol	Value	Unit
Material specifications	Resistivity	$\rho_{conductor}$	$1.68 \cdot 10^{-8}$	$\Omega \cdot m$
	Cross-section	$S_{conductor}$	640	mm^2
	Cost	$c_{conductor}$	8.5	€/kg
Design parameters	Number of coils	n_{coils}	6	-
	Turns per coil	$n_{turnsAC}$	40	-
	Average diameter per coil	$d_{ac,avg}$	400	mm
	Total length	$l_{conductor}$	302	m

4.2.2.3 AC coils

The device developed by Innopower is composed of six Alternating Current (AC) coils (two per phase), each with 40 turns. The coils were made of copper bars with a rectangular sectional area ($S_{conductor}$) of 64mm^2.

Regarding the lack of information on the dimensions of the AC coils, and considering the estimated diameter of each AC limb to be approximately 300 mm, the average diameter of each AC coil ($d_{AC,avg}$) was assumed to be 400 mm.

Therefore, the total length of cooper ($l_{conductor}$) required to manufacture the 6 AC coils was estimated to be approximately 302 m.

Table 4.6 shows the the parameters of the AC coils used for this study.

4.2.2.4 Cryogenic system

The cryogenic system developed by Innopower is based on an open-cycle cooling system. However, in this study, a closed-cycle system was considered, as the device is intended for long-term operation in the grid, making continuous LN_2 refilling impractical.

Regardless of the change in the cooling system configuration, the main design parameters of the dewar (cryostat) were maintained. The dewar has an annular cylindrical geometry and is fabricated from 304 stainless steel. To minimize heat leakage, a high-vacuum environment and multilayer insulation was applied, typically consisting of alternating layers of aluminum foil and glass fiber paper. Additionally, it comprises two current leads.

The design parameters of the dewar are shown in Table 4.7

Since the cooling system is closed-cycle, a cryocooler was integrated into the design. Its specifications were determined based on the estimated total heat input, which results mainly from thermal leakage through the dewar (cryostat and current leads).

Table 4.7: Parameters of the dewar.

	Parameters	Symbol	Value	Unit
Material specifications	Thermal Conductivity	k	$1.4 \cdot 10^{-3}$	$W/m \cdot K$
Design specifications	Height	h_{cryo}	1,160	mm
	Inner diameter	$d_{in,cryo}$	1,160	mm
	Outer diameter	$d_{out,cryo}$	1,511	mm
	Volume	V_{cryo}	434	L

The cost of the cryogenic system was considered to be 750 k€, excluding the additional cost of the cryocooler.

4.2.3 Loss estimation

The total core losses of the iron cores (P_{cores}) were calculated based on the estimated mass of B30P105 grain-oriented silicon steel presented in Section 4.2.2.1, and the specified core loss value for B30P105 at 1.7 T and 50 Hz (P_{core}).

The Joule losses in the AC coils (P_{jAC}) were calculated considering the total length of copper ($l_{conductor}$) required for their construction and the rated operating current of the device (I_r), which is approximately 1.5 kA.

According to the design's literature [64], the LN_2 consumption of the system, under zero magnetization current in the DC bias coil, is approximately 80 liters per day. This corresponds to a heat input of around 150 W, based on a LN_2 vaporization rate of 18.2 kg/kWh (around 22.48 L/kWh). When the magnetization current (I_{DC}) was increased to 150 A, the consumption rose by 20%, resulting in a heat input of 180 W—nearly equal to the value observed under on-grid operation. Therefore, 180 W was assumed as the total heat input of the device.

Considering the estimated heat input, the closed-cycle cooling system was modeled using the Gifford-McMahon Cryocooler AL-300 from Cryomech [65]. This cryocooler model has a cooling capacity (P_{th}) of 266 W at 80 K when operating at 50 Hz. Its input power consumption at this frequency is 7.0 kW for the water-cooled version and 7.6 kW for the air-cooled version. For this study, the water-cooled configuration was adopted, resulting in an effective efficiency of approximately 3.8%. The cost of the device was estimated to be approximately 40 k€.

The losses associated with the SIC-SFCL are summarize in Table 4.8.

Table 4.8: Losses of the SIC-SFCL.

Losses	**Value (kW)**
Iron cores	33
AC coils	18
Cryocooler	7
Total	58

4.2.4 CAPEX and OPEX estimation

The Capital Expenditure (CAPEX) of the superconducting device is summarized in Table 4.9. The estimation includes not only the cost of each main component of the device, but also the associated expenses for construction, manufacturing, assembly, and testing of the complete system. For the purpose of this analysis, these additional costs were assumed to represent 50% of the total cost of the main components.

Table 4.9: CAPEX of the SIC-SFCL.

CAPEX	**Value (k€)**
Iron Cores	92
HTS Coil	264
AC coils	3
Cryogenic system	790
Construction, manufacturing, assembly and testing	575
Total	1,724

The Operational Expenditure (OPEX) of the three-phase SIC-SFCL was calculated considering an electricity price of 53 €/MWh, corresponding to the 2024 yearly average market price reported by Rede Energia Nacional (REN) [66], and assuming continuous operation over 8,760 hours per year. In addition, the annual maintenance cost was estimated at 5% of the device's total CAPEX.

Table 4.10 summarizes the OPEX of the device.

Table 4.10: OPEX of the SIC-SFCL.

OPEX	**Value (k€/year)**
Maintenance	86
Yearly energy loss cost	27
Total	113

4.2.5 Economic analysis: Upgrading grid protection vs SIC-SFCL integration

This section presents the results of the economic comparison between the two solutions: upgrading the grid protection system and integrating a SIC-SFCL.

4.2.5.1 Investment Requirements for Grid Protection Upgrades

As previously mentioned, the SIC-SFCL is intended to be installed at the grid connection substation that links a future 63 MW DFIG-based wind farm to the Portuguese distribution grid at the Varosa substation.

Since the integration of the wind farm causes the I_{sc} at the Varosa substation to exceed its protection breaking capacity of 25 kA, it becomes necessary to estimate the cost of upgrading the breaking capacity of its protection devices to the next available rating of 31.5 kA.

To estimate these costs, the replacement cost of a 25 kA bay was considered, increased by 15%, resulting in a total of 460 k€ per bay.

The Varosa substation comprises eight high-voltage circuit-breakers, and therefore eight 25 kA bays. Based on this information, the total cost of upgrading the grid protection of the Varosa substation to a rated breaking capacity of 31.5 kA is estimated at 3,680 k€.

For the maintenance of the high-voltage switchgear, a cost of 5k€ per bay per year was considered, resulting in a total annual cost of 40k€.

4.2.5.2 Evaluation of Economic Performance Indicator

To assess the economic performance of both upgrading the grid protection and integrating a SIC-SFCL, a sensitivity analysis regarding the evaluation of the Life-cycle cost (LCC) indicator was performed for each solution.

The analysis considered three discount rates: 0%, 5%, and 10%. The 0% rate serves as a baseline case, where future costs are valued equally to present costs. The 5% rate represents a typical value used in energy sector investment studies, reflecting moderate risk and regulatory perspectives associated with conventional grid infrastructure projects. Finally, the 10% rate accounts for the greater uncertainty and risk associated with the adoption of emerging technologies.

For this analysis, a time horizon of 30 years was defined, based on the assumed lifetime of the SIC-SFCL system. To also capture short and medium-term perspectives of both solutions, two additional evaluations were conducted for 10 and 20 year periods.

Table 4.11 presents the results of the sensitivity analysis conducted to compare the economic performance of the two proposed solutions. It reports the LCC of both alternatives, along with the cost savings achieved by integrating the SIC-SFCL compared to upgrading the protection devices—expressed both in absolute monetary terms and as a percentage.

Table 4.11: Sensitivity analysis

Time Horizon (years)	**Discount Rate (%)**	**LCC — Upgrade Protection (k€)**	**LCC — SIC-SFCL (k€)**	**Savings (k€)**	**Savings (%)**
10	0	4,040	2,749	1,291	32
	5	3,776	2,416	1,360	36
	10	3,555	2,168	1,387	39
20	0	4,440	3,875	565	13
	5	3,965	2,949	1,016	26
	10	3,650	2,434	1,216	33
30	0	4,840	5,000	-160	-3
	5	4,082	3,277	805	20
	10	3,686	2,537	1,149	31

5

Conclusion and future work

5.1 Final review

In recent years, many Superconducting Fault Current Limiters (SFCLs) projects have been developed, and its technical feasibility in limiting short-circuit currents under real grid conditions has been successfully demonstrated. However, for this new technology to progress towards full commercial deployment, it is essential to prove it is economically feasible and competitive when compared with conventional grid reinforcement solutions.

This dissertation was conceived as an initial step towards the full commercialization of SFCLs. To this end, a Techno-Economic Assessment (TEA) of a Saturated Iron Cores Superconducting Fault Current Limiter (SIC-SFCL) was performed. The study focused on the integration of a Doubly-Fed Induction Generator (DFIG)-based wind farm into the Portuguese distribution network at the Varosa substation. The main objective was to evaluate whether the implementation of a SIC-SFCL would represent not only a better technical solution but, more importantly, a more economically feasible alternative when compared with upgrading the grid protection systems to the next short-circuit breaking capacity level.

After analyzing the short-circuit current contribution of the integrated wind farm, which enabled the estimation of the required grid specifications for the SIC-SFCL, an efficient methodology was developed to perform a TEA of the superconducting device. Within this methodology, the cost of all major components was assessed by first determining the required quantities and materials necessary for the manufacturing of the device under study, in order to estimate the Capital Expenditure (CAPEX) of the device. The losses of the device were also estimated, which allowed for the assessment its Operational Expenditure (OPEX).

The SIC-SFCL model designed use to conduct this study was the three-phase 35 kV/ 90 MVA SIC-SFCL designed by Innopower. Considering the original design, a few adjustments to the materials used (considering not only the lack of data but also the use of more advanced and developed material, like the 2G High Temperature Superconductor

(HTS) tape), and some assumptions regarding the cost of the cryogenic system, the total CAPEX of the design (considering some extra expenses like construction, manufacturing, assembly and testing) was estimated to be 1,724 k€, while the OPEX was estimated to be 113 k€ per year.

The alternative of upgrading the protection breaking capacity at the Varosa substation from 25 kA to 31.5 kA was considered with an assumed CAPEX of approximately 3,680 k€ and an annual OPEX of about 40 k€ for maintenance.

The sensitivity analysis performed through Life-cycle cost (LCC) evaluation of both solutions shows that, for a 10-year timeline horizon, the SIC-SFCL consistently provides lower costs compared to the conventional protection upgrade. In this case, savings range between 32% and 39%, corresponding to reductions of 1,291–1,387 k€. For a 20-year timeline horizon, the economic advantage of the SIC-SFCL remains, although at a smaller scale, with savings of between 13% and 33% (565–1,216 k€). For a 30-year horizon, the results become more sensitive to the discount rate: at 0% the conventional protection upgrade becomes more favorable, being 160 k€ (3%) less costly, whereas at 5% and 10% the integration of the SIC-SFCL reflects savings of 20% to 31% (805–1,149 k€).

Overall, the analysis indicates that under most scenarios, the integration of the SIC-SFCL represents a more cost-effective solution compared to upgrading protection devices.

5.2 Future work

The study presented in this document can be considered as a starting point for the implementation of a SIC-SFCL in power systems, given that SFCLs are still at the stage of economic feasibility studies and that no comprehensive techno-economic assessments of the device have yet been conducted.

In order to strengthen the demonstration of both the technical and economic feasibility of the superconducting device, future work should address the following aspects:

- The development of TEA based on updated SIC-SFCL designs specifically designed to meet the requirements of the target grid. This should take into account updated material costs, recent technological advances in superconductivity, and optimized device configurations, given that the prototype analyzed in this study was originally designed and manufactured in the early 2000s.
- The evaluation of the SIC-SFCL under different grid specifications should also be considered. For example, instead of installing the device at the distribution network level, it could be implemented within the transmission network. This would be essential to evaluate both the technical and economic feasibility of deploying the SFCL at higher voltage levels, as well as in different applications and locations within the grid.

Bibliography

[1] International Energy Agency. *Electricity Mid-Year Update 2025*. Licence: CC BY 4.0. Paris: International Energy Agency, 2025-07. URL: https://www.iea.org/reports/electricity-mid-year-update-2025 (visited on 2025-08-26) (cit. on p. 1).

[2] REN — Redes Energéticas Nacionais, S.A. *Electricity consumption grows 3.8% in July with solar setting a new record*. https://www.ren.pt/en-gb/media/news/electricity-consumption-grows-38-in-july-with-solar-setting-a-new-record. Accessed 2025-08-26. 2025-08 (cit. on p. 1).

[3] E. Graham, N. Fulghum, and K. Altieri. *Global Electricity Review 2025*. Creative Commons BY 4.0. Ember, 2025-04-08. URL: https://ember-energy.org/latest-insights/global-electricity-review-2025/ (visited on 2025-08-26) (cit. on p. 1).

[4] EDP — Energias de Portugal, S.A. *O novo plano de negócios em 12 perguntas*. Histórias EDP. URL: https://www.edp.com/pt/midia/historias-edp/o-novo-plano-de-negocios-em-12-perguntas (visited on 2025-08-26) (cit. on p. 1).

[5] D. Wu et al. "Assessing impact of renewable energy integration on system strength using site-dependent short circuit ratio". In: *IEEE Transactions on Sustainable Energy* 9.3 (2017), pp. 1072–1080 (cit. on p. 1).

[6] Y. Xin et al. "Development of superconducting fault current limiters". In: (2006), pp. 1–5 (cit. on pp. 1, 8, 12).

[7] W. Paul et al. "Fault current limiter based on high temperature superconductors–different concepts, test results, simulations, applications". In: *Physica C: Superconductivity* 354.1-4 (2001), pp. 27–33 (cit. on p. 4).

[8] Ł. Kozarek et al. "Impact of the short-circuit current value on the operation of overhead connections in high-voltage power stations". In: *Energies* 16.8 (2023), p. 3462 (cit. on p. 4).

[9] B. de Metz-Noblat, F. Dumas, and C. Poulain. “Calculation of short-circuit currents”. In: *Cahier technique* 158 (2005) (cit. on pp. 4, 6, 25).

[10] L. Kovalsky et al. “Applications of superconducting fault current limiters in electric power transmission systems”. In: *IEEE Transactions on Applied Superconductivity* 15.2 (2005), pp. 2130–2133 (cit. on p. 6).

[11] M. Noe and M. Steurer. “High-temperature superconductor fault current limiters: concepts, applications, and development status”. In: *Superconductor science and technology* 20.3 (2007), R15 (cit. on pp. 6, 8, 12, 14–16).

[12] S. Kalsi and A. Malozemoff. “HTS fault current limiter concept”. In: (2004), 1426–1430 Vol.2. DOI: 10.1109/PES.2004.1373103 (cit. on p. 7).

[13] M. Noe and B. Oswald. “Technical and economical benefits of superconducting fault current limiters in power systems”. In: *IEEE Transactions on applied superconductivity* 9.2 (1999), pp. 1347–1350 (cit. on p. 7).

[14] H. Schmitt. “Fault current limiters report on the activities of CIGRE WG A3. 16”. In: *2006 IEEE Power Engineering Society General Meeting*. IEEE. 2006, 5–pp (cit. on p. 7).

[15] E. Leung. “Superconducting fault current limiters”. In: *IEEE Power Engineering Review* 20.8 (2000), pp. 15–18. DOI: 10.1109/39.857449 (cit. on p. 8).

[16] H. K. Onnes. *The liquefaction of helium*. Springer, 1991, pp. 164–187 (cit. on p. 8).

[17] H. Kamerlingh Onnes. “Further experiments with liquid helium. G. On the electrical resistance of pure metals etc. VI. On the Sudden Change in the Rate at which the Resistance of Mercury Disappears”. In: *Proceedings of the Royal Netherlands Academy of Arts and Sciences* 14 II (1912), pp. 818–821 (cit. on p. 9).

[18] A. M. Forrest. “Meissner and Ochsenfeld revisited”. In: *European Journal of Physics* 4.2 (1983), p. 117 (cit. on p. 9).

[19] W. T. B. de Sousa. “Transient simulations of superconducting fault current limiters”. In: *Diss. Ph. D. dissertation, Dept. Elect. Eng, Federal University of Rio de Janeiro, Brazil* (2015) (cit. on pp. 10, 11).

[20] J. Bednorz and K. Müller. “Possible high T_c superconductivity in the Ba-La-Cu-O system”. In: *Z. Physik B - Condensed Matter* 64 (1986), pp. 189–193 (cit. on p. 10).

[21] J. S. Lamas et al. “Electrical and magnetic characterization of BSCCO and YBCO HTS tapes for fault current limiter application”. In: *IEEE transactions on Applied Superconductivity* 21.3 (2011), pp. 3398–3402 (cit. on p. 11).

[22] J. F. Gieras. “Superconducting electrical machines-State of the art”. In: *Organ* 12.9 (2009), pp. 4–25 (cit. on p. 11).

[23] *2G HTS Wire Specification*. SuperPower Inc. URL: https://www.superpower-inc.com/specification.aspx (visited on 2025-08-21) (cit. on p. 12).

[24] Y. Jia et al. “Numerical Simulation and Analysis of a Saturated-Core-Type Superconducting Fault Current Limiter”. In: *IEEE Transactions on Applied Superconductivity* 27.4 (2017), pp. 1–5. DOI: 10.1109/TASC.2017.2656619 (cit. on p. 15).

[25] Y. Xin et al. “Development of saturated iron core HTS fault current limiters”. In: *IEEE Transactions on Applied Superconductivity* 17.2 (2007), pp. 1760–1763 (cit. on p. 15).

[26] A. Morandi. “State of the art of superconducting fault current limiters and their application to the electric power system”. In: *Physica C: Superconductivity* 484 (2013), pp. 242–247 (cit. on p. 15).

[27] G. G. Sotelo et al. “A review of superconducting fault current limiters compared with other proven technologies”. In: *Superconductivity* 3 (2022), p. 100018 (cit. on p. 16).

[28] M. Noe et al. “Conceptual design of a 24 kV, 1 kA resistive superconducting fault current limiter”. In: *IEEE Transactions on applied superconductivity* 22.3 (2011), pp. 5600304–5600304 (cit. on pp. 16, 17).

[29] A. Colmenar-Santos et al. “Performance analysis of a superconducting fault current limiter in a power distribution substation”. In: *Electric Power Systems Research* 136 (2016), pp. 89–99 (cit. on p. 16).

[30] W. Paul et al. “Test of 1.2 MVA high-superconducting fault current limiter”. In: *Superconductor Science and Technology* 10.12 (1997), p. 914 (cit. on p. 17).

[31] Y. Xin et al. “Manufacturing and test of a 35 kV/90 MVA saturated iron-core type superconductive fault current limiter for live-grid operation”. In: *IEEE Transactions on Applied Superconductivity* 19.3 (2009), pp. 1934–1937 (cit. on pp. 17, 29, 48).

[32] Y. Xin et al. “Field tests on a 35kV/90MVA superconducting fault current limiter”. In: *2010 International Conference on Power System Technology*. IEEE. 2010, pp. 1–5 (cit. on p. 17).

[33] Y. Xin et al. “Development of a 220 kV/300 MVA superconductive fault current limiter”. In: *Superconductor Science and Technology* 25.10 (2012), p. 105011 (cit. on pp. 17, 18).

[34] Y. Xin et al. “Factory and field tests of a 220 kV/300 MVA statured iron-core superconducting fault current limiter”. In: *IEEE Transactions on Applied Superconductivity* 23.3 (2012), pp. 5602305–5602305 (cit. on p. 18).

[35] J. Bock et al. “CURL 10: development and field-test of a 10 kV/10 MVA resistive current limiter based on bulk MCP-BSCCO 2212”. In: *IEEE Transactions on Applied Superconductivity* 15.2 (2005), pp. 1955–1960. DOI: 10.1109/TASC.2005.849344 (cit. on p. 19).

[36] M. Moyzykh et al. “First Russian 220 kV superconducting fault current limiter (SFCL) for application in city grid”. In: *IEEE Transactions on Applied Superconductivity* 31.5 (2021), pp. 1–7 (cit. on p. 19).

[37] J. Kozak, M. Majka, and S. Kozak. “Experimental Results of a 15 kV, 140 A Superconducting Fault Current Limiter”. In: *IEEE Transactions on Applied Superconductivity* 27.4 (2017), pp. 1–4. DOI: 10.1109/TASC.2017.2651120 (cit. on p. 19).

[38] T. Ma et al. “Electromagnetic Design of High-Temperature Superconducting DC Bias Winding for Single-Phase 500 kV Saturated Iron-Core Fault Current Limiter”. In: *IEEE Transactions on Applied Superconductivity* 28.3 (2018), pp. 1–5. DOI: 10.1109/TASC.2017.2777877 (cit. on p. 19).

[39] C. Li et al. “Cooling unit for the 500 kV saturated iron core fault current limiter”. In: *IEEE transactions on applied superconductivity* 29.5 (2019), pp. 1–5 (cit. on pp. 19, 32, 35).

[40] E-REDES - Distribuição de Eletricidade, S.A. *Caracterização das Redes de Distribuição a 31 de dezembro de 2023*. Tech. rep. Acesso em: 24 abril 2025. E-REDES, 2023-abril. URL: https://www.e-redes.pt/pt-pt/caracterizacao-das-redes-de-distribuicao-3 (cit. on pp. 21, 23, 64, 65).

[41] Redes Energéticas Nacionais. *Caracterização da Rede Nacional de Transporte – Dados Técnicos*. Acesso em: 29 de abril de 2025. 2023. URL: https://datahub.ren.pt/pt/redes/?date=2023-12-31 (cit. on pp. 21, 64).

[42] Cabelte, S.A. *Catálogo Geral Cabelte 2023*. https://www.caiado.pt/images/uploaded/CatalogosCaiado/catalogo-cabelte-2023.pdf. Distribuído por Caiado S.A. 2023 (cit. on pp. 23, 65).

[43] Prysmian Group. *TransPowr® ACSR Bare Overhead Conductor (Canada)*. Technical datasheet for aluminum conductor steel-reinforced (ACSR) overhead conductors compliant with CAN/CSA C61089 standards. 2025 (cit. on pp. 23, 65).

[44] North American Transmission Forum. *Power Flow Modeling Reference Document*. Technical Report Version 1.1.1. Published June 2013; Copyright © 2013 North American Transmission Forum; Not for sale or commercial use; all rights reserved. North American Transmission Forum, 2013-06 (cit. on p. 24).

[45] European Network of Transmission System Operators for Electricity (ENTSO-E). *Short Circuit Contribution of New Generating Units Connected With Power Electronics and Protection Behaviour*. Technical Report. Brussels, Belgium. ENTSO-E, 2019-04 (cit. on p. 26).

[46] J. Yin, X. Huang, and W. Qian. “Analysis and research on short-circuit current characteristics and grid access faults of wind farms with multi-type fans”. In: *Energy Reports* 11 (2024), pp. 1161–1170 (cit. on p. 26).

[47] E. Muljadi et al. "Short circuit current contribution for different wind turbine generator types". In: *IEEE PES general meeting*. IEEE. 2010, pp. 1–8 (cit. on p. 26).

[48] Z. Wei et al. "Optimized design of coils and iron cores for a saturated iron core superconducting fault current limiter". In: *IEEE Transactions on Applied Superconductivity* 26.7 (2016), pp. 1–4 (cit. on p. 28).

[49] J. Y. Zhang et al. "Electromagnetic design of saturated iron core SFCL". In: *2011 International Conference on Applied Superconductivity and Electromagnetic Devices*. IEEE. 2011, pp. 305–308 (cit. on p. 28).

[50] N. Vilhena et al. "A design methodology for the optimization of three-phase SFCL of saturated cores type". In: *Ieee transactions on applied superconductivity* 28.4 (2018), pp. 1–5 (cit. on p. 28).

[51] J. W. Moscrop. "Experimental analysis of the magnetic flux characteristics of saturated core fault current limiters". In: *IEEE transactions on magnetics* 49.2 (2012), pp. 874–882 (cit. on p. 28).

[52] L. Bidoia. "Price of electrical steel sheets in the spotlight for EU buyers". In: *PricePedia Magazine* (2024-4 15). URL: https://www.pricepedia.it/en/magazine/article/2024/04/15/price-of-electrical-sheet-at-the-centre-of-attention-of-european-buyers/ (cit. on p. 28).

[53] K. Wang et al. "Advances in second-generation high-temperature superconducting tapes and their applications in high-field magnets". In: *Soft Science* 2.3 (2022), N–A (cit. on p. 30).

[54] J. Moscrop and F. Darmann. "Design and development of a 3-phase saturated core high temperature superconducting fault current limiter". In: *2009 International Conference on Electric Power and Energy Conversion Systems,(EPECS)*. IEEE. 2009, pp. 1–6 (cit. on p. 31).

[55] H. Hong et al. "Design, fabrication, and operation of the cryogenic system for a 220 kV/300 MVA saturated iron-core superconducting fault current limiter". In: *IEEE Transactions on Applied Superconductivity* 24.5 (2014), pp. 1–4 (cit. on pp. 32, 33).

[56] A. Ballarino. "Current leads, links and buses". In: *arXiv preprint arXiv:1501.07166* (2015) (cit. on pp. 32, 35).

[57] S. Yoshida. "Cryogenic cooling system for HTS cable". In: *Progress in Superconductivity and Cryogenics (PSAC)* 19.2 (2017), pp. 1–8 (cit. on p. 33).

[58] R. Radenbaugh. "Refrigeration for superconductors". In: *Proceedings of the IEEE* 92.10 (2004), pp. 1719–1734 (cit. on p. 33).

[59] M. Green. "The cost of coolers for cooling superconducting devices at temperatures at 4.2 K, 20 K, 40 K and 77 K". In: *IOP Conference Series: Materials Science and Engineering*. Vol. 101. 1. IOP Publishing. 2015, p. 012001 (cit. on p. 33).

[60] M. J. Kim et al. "Current-lead design for variable electric current in HTS power applications". In: *IEEE Transactions on Applied Superconductivity* 20.3 (2010), pp. 1725–1728 (cit. on p. 35).

[61] M. Furuse, K. Agatsuma, and S. Fuchino. "Evaluation of loss of current leads for HTS power apparatuses". In: *Cryogenics* 49.6 (2009), pp. 263–266 (cit. on p. 35).

[62] E-Redes. *PDIRD-E 2024*. `https://www.e-redes.pt/sites/eredes/files/`. Technical document of E-Redes regarding the Distribution Network Development Plan. 2024 (cit. on p. 36).

[63] L. Quéval. *Techno-Economic Assessment Guidelines (v20230502)*. Working Group 4 Deliverable. Working Group 4: Economic and Sustainability Assessment. Hi-SCALE COST Action CA19108, 2023-05. URL: `https://hi-scale.eu/deliverables/` (cit. on p. 37).

[64] H. Hong et al. "CRYOGENIC SYSTEM FOR A 35 KV/90 MVA SATURATED IRON-CORE SUPERCONDUCTING FAULT CURRENT LIMITER". In: *AIP Conference Proceedings*. Vol. 1218. 1. American Institute of Physics. 2010, pp. 1395–1401 (cit. on p. 52).

[65] Bluefors. *Cryomech Products*. `https://bluefors.com/products/cryomech-products/`. Accessed: 2025-09-30. 2025 (cit. on p. 52).

[66] *Electricity – Market*. `https://datahub.ren.pt/en/electricity/market/`. Accessed: 6 September 2025. 2025 (cit. on p. 53).

[67] *Transformadores de Potência: Transformadores trifásicos, de 60 kV/MT. Características e ensaios*. Especificação Técnica DMA-C52-140/N. Anula e substitui a edição de novembro de 2014. Lisboa: EDP Distribuição – Energia, S.A., DIT – Direção de Inovação e Desenvolvimento Tecnológico, 2020-05 (cit. on p. 66).

I

Complementary information regarding the methodology

Table I.1: Characteristics of the Varosa substation (adapted from [40]).

Substation	HV/MV (kV)	Total capacity (MVA)	Peak Power (MW)	S_{sc} (MVA)	I_{sc} (kA)	Breaking capacity (kA)
Varosa	60/30	45	31.8	2,478	23.845	25

Table I.2: Transformers at the Valdigem's substation (adapted from [41]).

Transformers	Voltages prim/sec (kV)	Nominal Power (MVA)	R (pu)	X (pu)	G (pu)	B (pu)
TRF 1	220/60	170	0.0026	0.1849	0.0004	-0.0006
TRF 2	220/60	170	0.0027	0.1826	0.0005	-0.0017
TRF 3	220/60	126	0.0035	0.1151	0.0004	-0.0030

Table I.3: Transmission lines of the grid under study (adapted from [40]).

Code	Name	Conductor type	Length (km)	Max. Current (A)
LN60 1009	Valdigem (REN) - Telheira	2x3x1 AA 325	18.06	882
LN60 1016	Valdigem (REN) - Varosa I	2x3x1 AA 235	1.479	478
LN60 1017	Valdigem (REN) - Varosa II	2x3x1 AA 325	1.461	874
LN60 1014	Valdigem (REN) - Jorjais	2x3x1 AA 325	27.009	407
LN60 1429	Valdigem (REN) - Vila de Rua	1x3x1 AA 325	30.595	172
LN60 1018	Varosa - Telheira	1x3x1 AA 325	16.273	0
LN60 1005	Varosa - Pinhão	1x3x1 AA 215	24.763	142
LN60 1382	Varosa - Lamego	1x3x1 AA 235	6.449	215
LN60 1062	Varosa - SS Seixinhos	1x3x1 AA 235	17.535	395
LN60 1493	SS Seixinhos - Carneiro	1x3x1 AA 245	9.494	232

Table I.4: Cable characteristics (adapted from [42, 43]).

Type	Cross-Section (mm^2)	Resistance (Ω/km)		Inductance (mH/km)	Capacitance (μF/km)
		DC 20ºC	AC 75ºC		
ACSR	215	0.1421	0.1742	0.8951	0.0192
	235	0.1411	0.1726	0.8709	0.0195
	245	0.1401	0.1726	0.8607	0.0196
	325	0.1007	0.1237	0.8314	0.0205

Table I.5: Loads of the grid's model .

Substations	Total Capacity (MVA)	P (MW)	Q (MVar)
Varosa	45	40.50	19.62
Telheira	63	56.70	27.46
Jorjais	31.5	28.35	13.73
Vila da Rua	31.5	28.35	13.73
Pinhão	30	27	13.08
Lamego	31.5	28.35	13.73
Carneiro	20	18	8.72

Table I.6: Standard characteristics of 60/30 kV power transformers used by E-REDES (adapted from [67]).

	S (MVA)	Z (%)
TRF1	20	10
TRF2	31.5	12.5
TRF3	40	15

Table I.7: Main specifications of the DFIG .

Parameters	**Value**	**Unit**
Wind turbine		
Rated Power	1.5	MW
Rated wind speed	12	m/s
DFIG		
Rated voltage	575	V
Nominal Power	1.6	MVA
Frequency	50	Hz
Stator Resitance	0.023	pu
Rotor Resistance	0.016	pu
Stator inductance	0.18	pu
Rotor inductance	0.16	pu
Mutual inductance	2.9	pu
Rotor initial speed	1.2	pu
DC-link voltage	1150	V
Number of poles	3	-